MALAYSIAN Journal of Catalysis

Vol. 8, No. 2, 2024 eISSN 0128-2581

Topics of journal (but are not limited to):

1. Catalytic Mechanisms
1-1. Spectroscopic and Visualizing Characterizations
1-2. Surface Chemistry, Reaction Kinetics and Mechanisms
1-3. Molecular Simulation and Theoretical Modeling
1-4. New Concepts for Catalysis

2. Catalytic Materials
2-1. Nanostructured Catalytic Materials
2-2. Micro- and Meso-Porous Catalytic Materials
2-3. Hybrid materials for catalysis

2-4. Novel Design and Synthetic Approaches

3. Catalysis for Energy
3-1. Efficient Utilization of Fossil Sources
3-2. Clean Energy Conversion: Electrocatalysis
3-3. Biomass Conversion
3-4. Photocatalysis for Hydrogen Production

4. Environmental Catalysis
4-1. Automotive Exhaust Cleanup
4-2. Water Pollution Control
4-3. Air Pollution Control
4-4. Updating and Utilization of Wastes

5. Catalysis for Chemical Synthesis
5-1. Green Synthesis
5-2. Petrochemicals
5-3. Fine Chemicals and Pharmaceuticals
5-4. Selective Oxidation & Hydrogenation

6. Cross-Disciplinary
6-1. Integration of Heterogeneous and Homogeneous
6-2. Organic and Biomimetic Catalysis
6-3. Industrial Catalysis
6-4. Other Surface Active Site Phenomena
6-5. Adsorption-Desorption Phenomena
6-6. Active sites Studies
6-7. Others

Faculty of Chemical and Energy Engineering
Universiti Teknologi Malaysia
http:/mjcat.utm.my/

Malaysian Journal of Catalysis 8 (2024) 36-43

Malaysian Journal of Catalysis
http://mjcat.utm.my/

MJCat
Research Article

Enhancing Aerobic Granular Sludge Formation in Domestic Wastewater Through Mg^{2+} Augmentation

Nurul Aqilah Abdullah Sani[1], Norhayati Abdullah[1*]

[1]*Algal Biomass iKohza, Chemical and Environmental Engineering (CHEE), Malaysia-Japan International Institute of Technology, Universiti Teknologi Malaysia, 54100 Kuala Lumpur*

**Corressponding Author*:*norhayati@utm.my*

Article history :
Received 8 August 2024
Accepted 7 November 2024

GRAPHICAL ABSTRACT

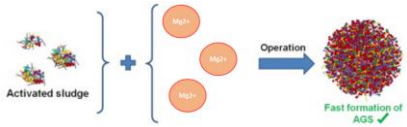

ABSTRACT

This study investigates the optimal Mg^{2+} concentration for enhancing aerobic granular sludge (AGS) formation in domestic wastewater treatment. Domestic wastewater and activated seed sludge samples were sourced from a local treatment plant, and three Mg^{2+} concentrations (130 mg/L, 160 mg/L, and 260 mg/L) were tested alongside a control sample without Mg^{2+}. Each sample was supplemented with magnesium sulfate and cultivated in four lab-scale sequential batch reactors. The reactor with 160 mg/L Mg^{2+} demonstrated the highest chemical oxygen demand (COD) removal efficiency (96.93%) and optimal granule stability due to an enhanced extracellular polymeric substance (EPS) production, specifically proteins. Higher concentrations (260 mg/L) caused EPS destabilization, negatively affecting granule formation. The 160 mg/L concentration provided the best balance for rapid AGS formation, settling, and COD removal, aligning with the literature on the role of divalent cations in sludge granulation. These findings present a promising approach for improving wastewater treatment efficiency through controlled Mg^{2+} augmentation.

Keywords: Mg^{2+} concentration, Aerobic Granular Sludge, Chemical Oxygen Demand, Extracellular Polymeric Substances, Wastewater treatment.

eISSN 0128-2581

1. INTRODUCTION

Wastewater treatment is essential for safeguarding the environment and public health by removing contaminants, reducing water pollution, and spreading waterborne diseases[1]. Biological treatment technology, which utilizes microorganisms like bacteria, fungi, and algae, provides a cost-effective and environmentally sustainable solution for efficiently breaking down organic matter and eliminating pollutants [2][3].

Activated sludge (AS) is a widely used biological treatment method in municipal and industrial wastewater treatment[4]. It is a suspended-growth process where a concentrated microbial culture degrades organic matter under aerobic conditions, forming biological flocs for sludge-water separation in a clarifier[5]. Activated sludge is highly efficient in treating BOD, COD, and other nutrients, producing high-quality effluent without harmful chemicals[6]. However, conventional activated sludge systems face limitations that impact their performance. The small size of activated granules results in a high surface area-to-volume ratio, which increases drag force and hampers effective settling. This decreases the settling velocity and retention time, complicating the sludge-liquid separation process and reducing effluent quality. Consequently, larger land footprints are required for additional clarifiers to separate solids [7].

Aerobic granular sludge (AGS) was introduced as a better alternative for solid-liquid separation. Under aerobic conditions, conventional activated sludge can form compact and dense AGS aggregates, enhancing settling velocity and reducing retention time[8]. AGS allows for higher biomass concentrations and simultaneous nitrification, denitrification, and phosphate removal in a single treatment tank, reducing land footprint by 50-70% and energy consumption by 30-48% compared to conventional methods[9].

Despite its advantages, AGS stability remains an issue. Mineral accumulation and increased granule sizes can lead to AGS collapse, reducing efficiency[10]. Factors such as temperature, pressure, microbial composition, C/N ratio, and wastewater type contribute to AGS instability,

necessitating constant adjustments[11]. Divalent metal ions like Fe^{2+}, Ca^{2+}, and Mg^{2+} have been shown to promote stable AGS formation, enhancing microbial aggregation and granulation[12].

While research on Mg^{2+} impact on AGS exists, it is somewhat outdated, and the results vary due to changes in wastewater characteristics and limited studies on varying Mg^{2+} concentrations. Most research has focused on synthetic wastewater, which lacks organic matter present in real wastewater. Furthermore, there were no specifications on the optimum Mg^{2+} range to improve aerobic respiration as well as the side effects of excessive Mg^{2+} addition.

This study aims to investigate the effect of different Mg^{2+} concentrations on AGS formation in domestic wastewater. The development of granules and settling abilities will be observed through analytical methods, and the extracellular polymeric substance (EPS) content of proteins will be analyzed to understand the impact of Mg^{2+} augmentation on granule stability.

2. EXPERIMENTS

2.1 Seed Sludge Sampling

Seed sludge was obtained from a local wastewater treatment plant by collecting activated sludge mixed with wastewater from the aeration tank using a plastic pail. This mixture was poured into a measuring cylinder for settling. After 30 minutes of settling, the top layer of wastewater was removed, and the thick activated sludge was transferred into polyethylene bottles using a plastic funnel. A total of 30 litres of sludge was obtained, filtered, and stored in a refrigerator at 4°C in the MJIIT lab.

2.2 Domestic Wastewater Sampling

The wastewater was sampled from the influent wastewater tank. The same plastic pail was used to collect the wastewater sample. A total of 45 litres of influent wastewater was collected into two polyethylene bottles. Both bottles were taken back to the lab and refrigerated at 4°C.

2.3 Wastewater Samples Preparation

In this experiment, three concentrations of Mg^{2+} were studied based on the range of metal ion concentrations utilized in past research on the cultivation of aerobic granular sludge. The concentrations used were 130 mg/L, 160 mg/L, and 260 mg/L of Mg^{2+}. Magnesium ion was obtained from solid magnesium sulfate ($MgSO_4$) due to its ability to readily dissolve in water, providing a reliable source of Mg^{2+} ions for the wastewater and promoting the production of extracellular polymeric substances (EPS) within granules.

The influent wastewater was mixed with $MgSO_4$ at the desired concentrations before the cultivation process. Each sample, mixed with magnesium sulfate, was kept separately and tagged with its specified concentration of 130 mg/L, 160 mg/L, and 260 mg/L. A fourth sample was prepared as a control with no addition of magnesium sulfate.

To produce wastewater solutions with different concentrations of Mg^{2+} ions, solid magnesium sulfate ($MgSO_4$) was weighed using analytical balance before being poured into the wastewater and mixed until completely dissolved. The required amount of magnesium sulfate for each concentration was calculated using Equation 1 as shown below:

$$C = \frac{n}{V} \quad (1)$$

Where C is the concentration (in moles per liter, M), n is the number of moles of solute, and V is the volume of solution in litres.

The Mg^{2+} concentrations of 130 mg/L, 160 mg/L, and 260 mg/L were selected based on existing studies and preliminary experiments. Research has shown that Mg^{2+} concentrations between 100 mg/L and 300 mg/L can significantly impact aerobic granular sludge (AGS) formation. Li et al. (2009) reported that concentrations within this range promote faster EPS production and better microbial aggregation. Preliminary trials in this study also indicated that 160 mg/L is particularly effective at maintaining granule stability without the adverse effects seen at higher concentrations like 260 mg/L

2.4 Reactor Set-Up and Operation

The cultivation of AGS was conducted using four identical sequencing batch reactors (SBR) offering flexibility in controlling the AGS formation process. Each reactor had a total volume of 3L, equipped with 2 running aeration pumps. The aeration pumps were set at 2.5 L/min for optimum microbial reactions. Reactors were set with two columns each, designated for different Mg^{2+} concentrations: control, 130 mg/L, 160 mg/L, and 260 mg/L. Wastewater samples were mixed with $MgSO_4$ beforehand to achieve the desired Mg^{2+} concentrations. The SBRs operated under a 3-hour cycle consisting of influent addition, aeration, settling, and effluent withdrawal, with a 15-minute idle period. The reactors were maintained at 18 °C in a controlled laboratory environment and operated for 20 days to observe AGS formation.

2.5 Volumetric Exchange Rate

All four reactors were seeded with a volumetric exchange rate of 50:50 sludge to wastewater ratio. The ratio is commonly used in developing aerobic granular sludge. The controlled reactor was seeded with 50% raw wastewater

and 50% activated sludge. Meanwhile, the experimental reactors were seeded with 50% activated sludge and 50% raw wastewater with the augmentation of 130 mg/L, 160 mg/L, and 260 mg/L Mg^{2+} respectively. All four reactors were aerated with the same type of air pump at the same flow rate for the SBR.

2.6 Chemical Oxygen Demand Analysis

To assess the impact of different Mg^{2+} concentrations on organic matter removal efficiency, Chemical Oxygen Demand (COD) analysis was conducted following the USEPA Reactor Digestion Method. After settling in the sequential batch reactor (SBR), effluent from the top layer was collected and divided into four labeled beakers representing control, 130 mg/L, 160 mg/L, and 260 mg/L samples.

During effluent collection, the DRB 200 Reactor was preheated to 150ºC. High-range HACH COD vials were labeled accordingly, including a blank sample prepared with distilled water. Each vial was filled with 2.00 mL of the respective sample or distilled water, with care taken to prevent burns from the exothermic reaction during vial handling.

After tightly closing the vial caps, they were gently inverted to mix the reagent. The prepared vials were then heated for two hours in the preheated DRB 200 reactor. Following heating, the reactor was switched off, and vials were left to cool for approximately 20 minutes.

Once cooled, COD values were measured using the DR3900 Laboratory VIS Spectrophotometer with the 435 COD HR program. The blank vial was inserted to zero the instrument, and then replaced with the control sample for reading. The process was repeated for experimental vials, and data were recorded accordingly.

2.7 Mixed Liquor Suspended Solids Analysis

Initially, the dry weight of an empty crucible was measured using an analytical balance, and the weights were recorded. One-litre samples of mixed liquor were obtained from all four SBRs using a measuring cylinder. Vacuum filtration was conducted using a vacuum pump connected to a vacuum flask with a filter membrane and an evaporating dish. The Whatman filter paper was placed in the filter holder and wetted with distilled water to secure the funnel. The mixed liquor samples were poured into the filter holder and filtered within 10 minutes, up to a maximum of 1 litre.

The filter and collected solids were washed with three successive 10 mL portions of distilled water to remove any dissolved solids. After filtration, the filter was dried in an oven set at 104±1°C for at least one hour. Once cooled, the filter was weighed, excluding the pan. This cycle of drying, cooling, desiccating, and weighing was repeated until a stable weight was obtained. Finally, MLSS values were calculated using Equation 2 as shown below.

$$\frac{weight\ final\ (g) - weight\ initial\ (g)}{sample\ volume\ (L)} = MLSS\ \left(\frac{g}{L}\right) \qquad (2)$$

2.8 Suspended Solids Analysis

Suspended solids were measured to calculate the sludge volume index (SVI). The suspended solids were measured using an Imhoff cone. One litre of mixed liquor samples was collected from the control, 130 mg/L, 160 mg/L, and 260 mg/L samples. The mixed liquor was filled into the Imhoff cone and left to settle for 45 minutes. The cone was moved forward and backward several times to ensure all the sediments settled down. After 45 minutes, the volume of settleable solids was recorded from the graduated scale at the top of the solid layer. All the settleable solids were recorded.

2.9 Sludge Volume Index (SVI) Analysis

From the measured MLSS and suspended solid, the sludge volume index was measured using this formula:

$$SVI\ \left(\frac{mL}{g}\right) = \frac{Settled\ sludge\ volume\ \left(\frac{mL}{L}\right)}{MLSS\ \left(\frac{g}{L}\right)}\ x\ 1000\ \left(\frac{mg}{g}\right) \qquad (3)$$

From the measured SVI value, a graph of SVI against time was plotted to study the settling characteristic of the sludge.

2.10 Granules Sieving Process

A sieving method was conducted to estimate the granule size distribution. The sludge sample was taken from the bottom of the sampling points for control, 130 mg/L, 160 mg/L and 260 mg/L reactors and each sludge sample was divided into four fractions using laboratory sieves with various diameters (0.2 mm, 0.6 mm, 1.0 mm, 1.5 mm). The sludge particles were gently submerged in water and shaken to let smaller particles pass through the openings. The procedure was repeated until all three sieves were utilized.

After sieving, the AGS collected on each sieve was weighed. The total mass of the sample was calculated by summing the weights of all size fractions. For each size fraction, the percentage of the total mass represented by that fraction was calculated by dividing the weight of the individual size fraction by the total mass and multiplying by 100. The results were then tabulated for each reactor.

2.11 Extracellular Polymeric Substance (EPS) Extraction and Analysis

To study the stability of granules cultivated, EPS extraction was carried out using the centrifugation method. First, 3g of sludge was extracted from each of the four SBR tanks and placed into centrifugation tubes. Demineralized

water was added to each tube, and the tubes were gently shaken by hand. The tubes were then centrifuged at 4000 rpm and 4°C for 20 minutes. The supernatant was collected in a glass beaker, and the pellet was discarded. The supernatant was used for protein analysis.

Protein (PN) estimation was performed using the modified Lowry method by FrØlund et al. (1995), with bovine serum albumin as the standard. This method was chosen for its clarity, effectiveness, and ability to maintain EPS integrity throughout the extraction process. The protein content of the granules represents the stability of the granules.

3. RESULTS AND DISCUSSION

COD content was successfully removed from the domestic wastewater in both control and experimental reactors, indicating positive microbial growth as the microorganisms consumed the organic material with the introduction of aeration. Table 1 lists the average effluent COD concentration and removal percentage in the four reactors after 20 days of operation.

Table 1 Average effluent COD concentration and Percentage of COD Removal in Reactors

Reactor	Average Effluent COD Concentration (mg/L)	Percentage of COD Removal (%)
Control	60.4	83.55
130 mg/L	55.3	85.71
160 mg/L	28.7	96.93
260 mg/L	30.4	96.26

After 20 days, reactors with varying Mg^{2+} concentrations showed improved organic matter removal efficiency. The reactor with 160 mg/L Mg^{2+} achieved the highest COD removal (96.93%), indicating Mg^{2+} augmentation's positive impact. Mg^{2+} facilitates coagulation and microbial aggregation, enhancing EPS secretion and COD removal efficiency. Initial rapid COD drops suggest microorganism starvation post-sampling. From day 2, stabilized COD removal patterns were observed, with Mg^{2+} augmented samples consistently showing lower effluent COD. Fig 1 and 2 illustrate the significant efficiency improvement, especially at 160 mg/L of Mg^{2+}. Mg^{2+} concentrations between 160 mg/L and 260 mg/L were identified as optimal for enhancing aerobic granular sludge formation and improving wastewater treatment efficacy.

The reactor with 160 mg/L of Mg^{2+} achieved the highest COD removal at 96.93%. This can be attributed to the fact that Mg^{2+} enhances microbial aggregation and EPS production, which improves the overall sludge structure and facilitates better substrate uptake [16]. Divalent metal ions

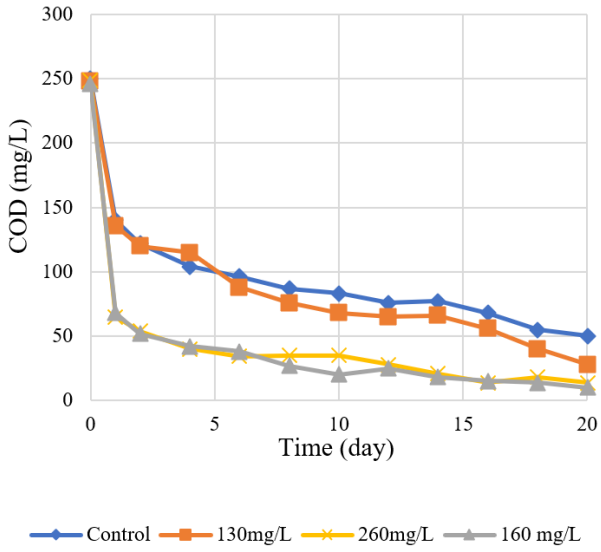

Fig. 1. Effluent COD value for (♦); control system (▲); 160 mg/L Mg^{2+} augmentation (■); 130 mg/L Mg^{2+} augmentation (×); 260 mg/L Mg^{2+} augmentation

like Mg^{2+} can interact with negatively charged EPS molecules, promoting tighter microbial floc formation, leading to faster and more efficient COD reduction [16]. The findings are consistent with Jiang et al. (2003) and X. M. Li et al. (2009), who reported that Mg^{2+} facilitates rapid granule formation and boosts microbial performance [15][16]. Higher concentrations like 260 mg/L, although effective, may result in diminishing returns due to an imbalance in EPS composition, thus making 160 mg/L the optimal concentration for enhanced COD removal.

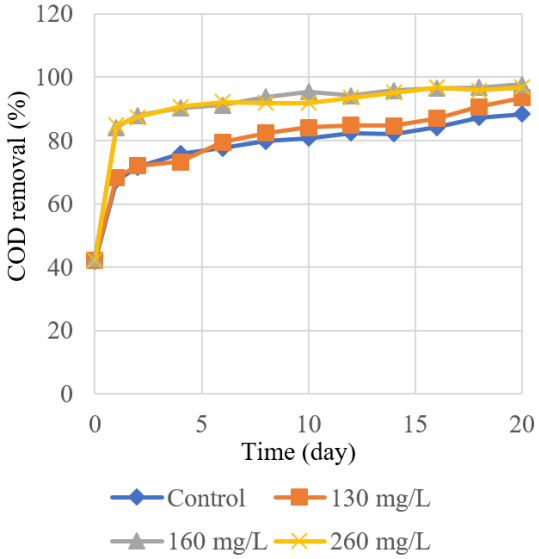

Fig. 2. COD removal percentage for (♦); control system (▲); 160 mg/L Mg^{2+} augmentation (■); 130 mg/L Mg^{2+} augmentation (×); 260 mg/L Mg^{2+} augmentation

The results of this study align with those of X. M. Li et al. (2009), who demonstrated that Mg^{2+} improves sludge settling and granule formation [16]. At concentrations around 160 mg/L, EPS production is optimal, leading to more compact and dense granules, which corresponds with the 96.93% COD removal observed here. Compared to lower concentrations like 130 mg/L, which exhibit delayed granulation, or higher concentrations like 260 mg/L, which cause EPS destabilization, 160 mg/L provides the best balance. This is further supported by Jiang et al. (2003), who also noted similar trends in metal ion augmentation for AGS formation [15].

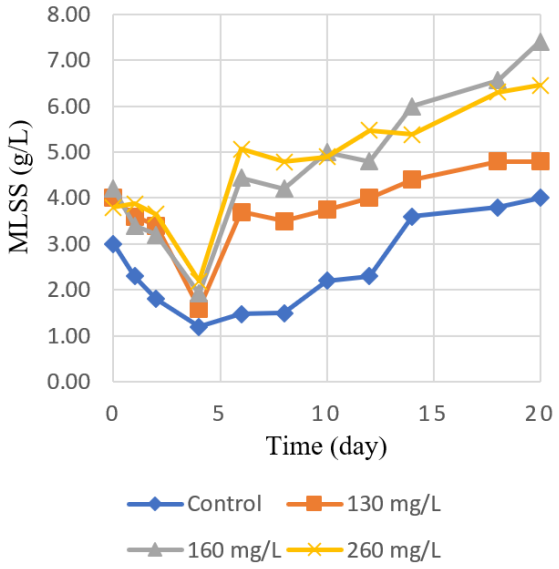

Fig. 3. MLSS value for (♦); control system (▲); 160 mg/L Mg^{2+} augmentation (■); 130 mg/L Mg^{2+} augmentation (×); 260 mg/L Mg^{2+} augmentation

Fig 3 shows the MLSS pattern throughout experiment. In the initial stages, the absence of aerobic granule formation results in low MLSS values across all samples, with biomass exhibiting a loose structure. Additionally, from day 0 to 4, low initial settling of activated sludge (AS) in the SBR leads to MLSS reduction as the AS trying to adapt to the new environment. Subsequently, sludge concentration fluctuates due to floc washout followed by granule dominance. After day 4, MLSS values increase significantly as activated sludge adapts and started to secrete EPS.

Among the three experimental samples the 160 mg/L shows the highest MLSS value near the end of cultivation compared to 130 mg/L and 260 mg/L samples. Interestingly, from day 4 until 12 the samples 260 mg/L reach the highest MLSS value compared to the others. At 260 mg/L, the Mg^{2+} concentration may be too high, leading to adverse effects on the AGS formation. High concentrations of divalent cations can disrupt the balance of extracellular polymeric substances (EPS) that are crucial for granule stability. This disruption can result in the disintegration of granules and a subsequent reduction in MLSS. Throughout the experiment, MLSS generally increases, with Mg^{2+} augmented reactors experiencing a more rapid rise compared to the control set, indicating Mg^{2+} 's positive impact on biomass concentrations and granular sludge settling characteristics in wastewater treatment.

Fig 4 illustrates the sludge volume index (SVI) for the four samples. Initially, SVI values slightly increased, peaking at 110 mL/g for the control set, indicative of disintegrated sludge structures hindering settling. However, after day 4, all samples exhibited decreased SVI values due to increased EPS secretion and granule compactness from the feast and famine cycle. Notably, the control set consistently had the highest SVI, suggesting slower settling without magnesium ions' positive charge interaction with organic matter. Furthermore, SVI showed an inverse relationship with MLSS, as increased MLSS over 20 days corresponded to decreased SVI, indicating improved settling with granule formation and reduced floc washout during drainage cycles, thereby increasing biomass content.

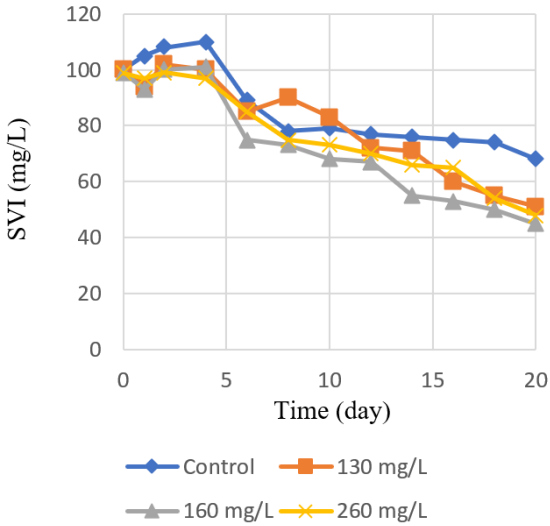

Fig. 4. SVI value for (♦); control system (▲); 160 mg/L Mg^{2+} augmentation (■); 130 mg/L Mg^{2+} augmentation (×); 260 mg/L Mg^{2+} augmentation

The slight increment in SVI observed at 130 mg/L after day 5 can be explained by incomplete granulation at this concentration. During the initial stages, flocs may still dominate over granules, causing less efficient settling. Magnesium ions at 130 mg/L may trigger EPS production but do not fully stabilize the granular structure, leading to higher SVI values compared to 160 mg/L, where granules are more compact. Previous studies have suggested that incomplete or unstable granulation can cause fluctuating SVI values.

The protein content (PN) in extracellular polymeric substance (EPS) is crucial for the sludge granules' stability as proteins have a high content of negatively charged amino acids, allowing them to form electrostatic bonds with multivalent cations like calcium and magnesium[13]. These bonds help stabilize the aggregate structure of granules. Based on the PN analysis results, all samples exhibited an increase in PN values over 20 days, attributed to the support provided by excess Mg^{2+} in polysaccharide formation within granules. Polysaccharides contribute to a robust framework essential for stable granular structure maintenance[14] . The interaction of polysaccharide functional groups, such as OH, with Mg^{2+} further enhances structural stability by forming a rigid, non-deformable polymeric gel-like matrix[14].

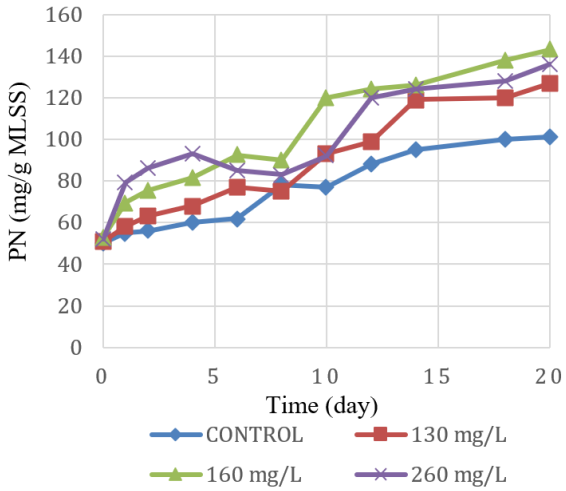

Fig. 5. PN value for (♦); control system (▲); 160 mg/L Mg^{2+} augmentation (■); 130 mg/L Mg^{2+} augmentation (×); 260 mg/L Mg^{2+} augmentation

The 160 mg/L reactor demonstrated the highest PN concentration at 143 mg/L, while the control reactor showed the lowest, slowing down the granulation process. Interestingly, despite higher Mg^{2+} concentration, the 260 mg/L reactor did not exhibit the highest PN content. Fig 5 highlights a significant drop in PN concentration on day 8 for the 260 mg/L reactor, indicating potential EPS composition alterations due to excessive Mg^{2+}. Thus, the optimal Mg^{2+} concentration for maximum PN content was observed at 160 mg/L, with concentrations above 260 mg/L potentially impacting EPS composition and reducing PN content, resulting in less compact and dense granules compared to those at 160 mg/L.

The granule size distribution analysis revealed significant insights into the effect of Mg^{2+} concentration on granule formation and maturation. Initially, the majority of granules in all reactors were below 0.2 mm, indicating early-stage development[14]. However, notable differences emerged over time. In the control reactor (Fig 6), granule growth was slow, with sizes mainly between 0.2 mm and 0.6 mm. This slow growth resulted in less dense granules, explaining the high SVI observed during the cultivation period.

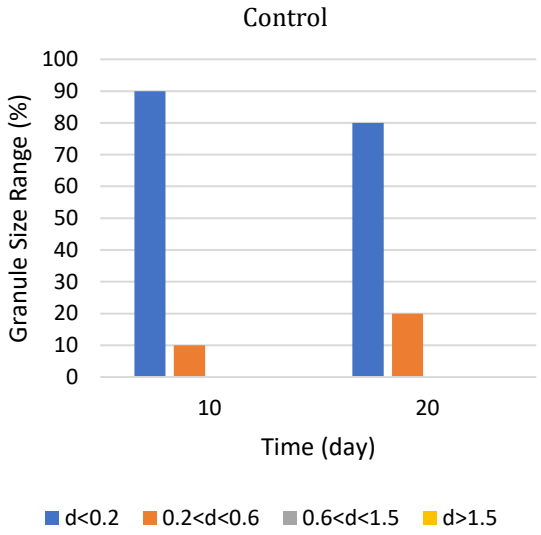

Fig. 6. Size distributions (by weight) of granules of control reactor A: d < 0.2; B: 0.2 < d < 0.6; C: 0.6 < d < 1.5; D: d > 1.5 (unit in mm)

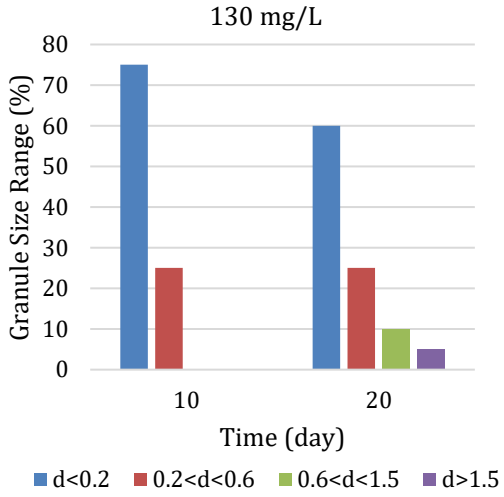

Fig. 7. Size distributions (by weight) of granules of 130 mg/L reactor A: d < 0.2; B: 0.2 < d < 0.6; C: 0.6 < d < 1.5; D: d > 1.5 (unit in mm)

Contrastingly, the 130 mg/L reactor (Fig 7) exhibited accelerated granule growth, surpassing the control reactor by achieving sizes larger than 0.6 mm within 10 days. This acceleration is attributed to magnesium ions stimulating higher EPS production, crucial for granule stabilization and maturation[15]. The 160 mg/L reactor (Fig 8) demonstrated the fastest granule growth, with mature structures above 0.6 mm within 10 days. By day 20, granules

above 1.5 mm constituted a significant percentage, indicating optimal conditions for rapid maturation. In the 260 mg/L reactor (Fig 9), granule growth was slightly slower than the 160 mg/L reactor, with a majority of granules below 0.2 mm. By day 20, however, granules above 0.6 mm increased, although growth rates were lower compared to the 160 mg/L reactor.

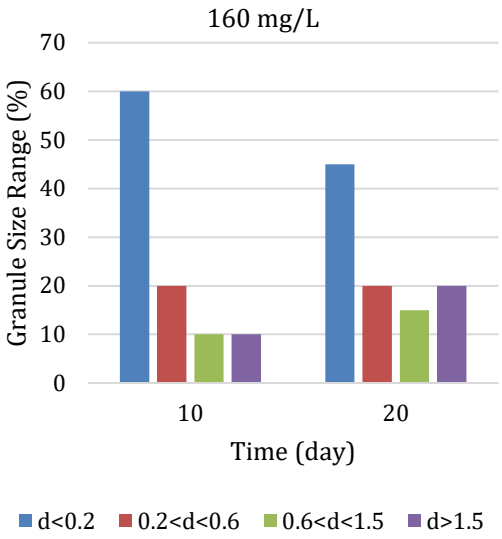

Fig. 8. Size distributions (by weight) of granules of 160mg/L reactor A: d < 0.2; B: 0.2 < d < 0.6; C: 0.6 < d < 1.5; D: d > 1.5 (unit in mm)

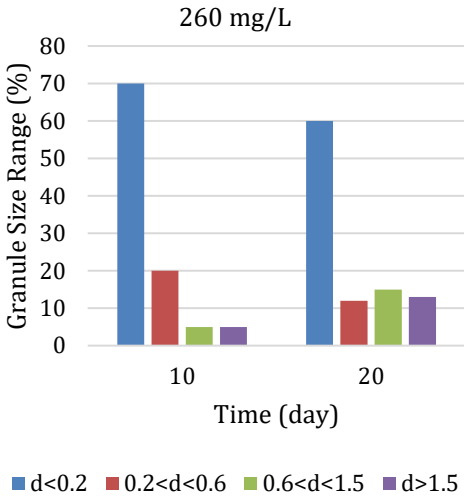

Fig. 9. Size distributions (by weight) of granules of 260 mg/L reactor A: d < 0.2; B: 0.2 < d < 0.6; C: 0.6 < d < 1.5; D: d > 1.5 (unit in mm)

Overall, Mg^{2+} presence accelerated granule formation and reduced maturation time [16]. However, concentrations exceeding 260 mg/L hindered growth, possibly due to EPS breakdown or microorganism respiration inhibition. Thus, Mg^{2+} facilitates earlier and larger aggregate formation, expediting sludge maturation within 20 days compared to the conventional 30 days.

In this study complete granulation of AGS is defined as achieving 15% of granules larger than 0.6 mm. Both the 160 mg/L and 260 mg/L reactors reached this threshold within 20 days, showing higher biomass concentration and earlier visible granules compared to the control and 130 mg/L reactors. The 130 mg/L reactor achieved 10% granules above 0.6 mm, indicating better growth than the control, which had none by day 20. These results indicate that Mg^{2+} concentrations between 160 and 260 mg/L significantly improve biomass retention and accelerate the granulation process.

4. CONCLUSION

This study demonstrates that Mg^{2+} concentration plays a critical role in enhancing aerobic granular sludge (AGS) formation and performance. The optimal Mg^{2+} concentration was found to be 160 mg/L, which yielded the highest COD removal efficiency (96.93%) and improved granule stability through enhanced extracellular polymeric substance (EPS) production, particularly proteins. The results showed that while 260 mg/L promoted early granulation, it led to EPS destabilization, indicating that excessive Mg^{2+} can negatively impact sludge stability. The 160 mg/L reactor consistently produced stable granules, reduced the sludge volume index (SVI), and accelerated granule formation from 30 to 20 days. This concentration provides a balance between rapid AGS formation and effective organic matter removal, aligning with findings from previous studies on the benefits of divalent cation augmentation in AGS systems. Future research could explore the combined effects of other metal ions like Ca^{2+} and Fe^{2+} to further enhance AGS performance. These findings offer valuable insights for optimizing wastewater treatment processes through precise Mg^{2+} dosing, contributing to more sustainable and cost-effective management practices.

ACKNOWLEDGEMENTS

This work was supported by a Collaborative Research Grant from Universiti Teknologi Malaysia (Q.K130000.2443.07G66).

REFERENCES

[1] Obaideen, K., Shehata, N., Sayed, E. T., Abdelkareem, M. A., Mahmoud, M. S., & Olabi, A. G. (2022). 7, 100112.https://doi.org/10.1016/J.NEXUS.2022.100112

[2] Zoomi, I., Kehri, H. K., Akhtar, O., Pandey, D., Singh, U., Chaudhary, K. L., & Narayan, R. P. (2021).

[3] Musa, M. A., & Idrus, S. (2021). 4656. https://doi.org/10.3390/SU13094656
[4] Hussain, A., Kumari, R., Sachan, S. G., & Sachan, A. (2021). 175–192. https://doi.org/10.1016/B978-0-12-822503-5.00002-3
[5] Wojnowska-Baryła, I., Stachowiak, D., & Klimiuk, E. (1996). 725–730. https://doi.org/10.1016/S0921-0423(96)80098-0.
[6] Stott, R. (2003). 491–521. https://doi.org/10.1016/B978-012470100-7/50032-7.
[7] Sharma, R., Verma, N., Lugani, Y., Kumar, S., & Asadnia, M. (2021). 1–48. https://doi.org/10.1016/B978-0-12-821883-9.00009-6.
[8] Nancharaiah, Y. V., & Sarvajith, M. (2019a). 12, 57–65. https://doi.org/10.1016/J.COESH.2019.09.011.
[9] Bengtsson, S., de Blois, M., Wilén, B. M., & Gustavsson, D. (2019). 40(21), 2769–2778. https://doi.org/10.1080/09593330.2018.1452985.
[10] Zou, J., Yang, J., He, H., Wang, X., Mei, R., Cai, L., & Li, J. (2022). 19(17). https://doi.org/10.3390/IJERPH191710940/S1.
[11] Hou, Y., Gan, C., Chen, R., Chen, Y., Yuan, S., & Chen, Y. (2021). 2726. https://doi.org/10.3390/W13192726.
[12] Jiang, H. L., Tay, J. H., Liu, Y., & Tay, S. T. L. (2003). 95–99. https://doi.org/10.1023/A:1021967914544/METRICS.
[13] Geng, M., You, S., Guo, H., Ma, F., Xiao, X., Zhang, J., & Ma, X. (2022). 1385–8947. https://doi.org/10.1016/j.cej.2022.136458.
[14] Hou, Y., Gan, C., Chen, R., Chen, Y., Yuan, S., & Chen, Y. (2021). 2726. https://doi.org/10.3390/W13192726.
[15] Maltos, R. A., Holloway, R. W., & Cath, T. Y. (2020). 250, 117214. https://doi.org/10.1016/J.SEPPUR.2020.117214.
[16] Li, X. M., Liu, Q. Q., Yang, Q., Guo, L., Zeng, G. M., Hu, J. M., & Zheng, W.(2009). 100(1), 64–67. https://doi.org/10.1016/J.BIORTECH.2008.06.015

Malaysian Journal of Catalysis 8 (2024) 44-49

Malaysian Journal of Catalysis
http://mjcat.utm.my/

MJCat
Research Article

Environmental Influences on Microplastics and Particulate Matter Resuspension in Indoor Air: A Study of Office Settings with Air Conditioning

Nor Haida Azwa Mohmad[1], NorRuwaida J[1*], Dewika M[2], Sara Y Y[3], Norfatiha I[1], Nur Aqilah Samsukamal[1]

[1] *Air Resources Research Laboratory, Malaysia-Japan International Institute of Technology Universiti Teknologi Malaysia*
[2] *Centre of American Education, Sunway University, Bandar Sunway, 47500, Selangor, Malaysia*
[3] *Faculty of Civil Engineering Technology, Universiti Malaysia Perlis, Kompleks Pusat Pengajian Jejawi, 02600, Jejawi Perlis, Malaysia*

**Corresponding Author: ruwaida.kl@utm.my*

Article history:
Received 8 August 2024
Accepted 3 November 2024

ABSTRACT

This study investigates airborne microplastics (MPs) in office environments, with a particular focus on spaces with air conditioning (AC), due to increasing health concerns. The research aims to analyze the physical characteristics, sources, distribution, and potential health risks of MPs. Despite growing awareness of MP pollution, comprehensive data on their specifics in office settings such as shape, composition, and size remain limited. Between November 2023 and January 2024, 42 air samples were collected under controlled conditions, both with and without AC, at the Air Resource Research Laboratory, Universiti Teknologi Malaysia Kuala Lumpur Campus. Stereomicroscopy was employed to identify the MPs' physical properties, revealing a dominance of bead-shaped MPs in air-conditioned spaces, with smaller particles (<50µm), often transparent or black, being the most prevalent. Environmental factors like wind speed and humidity were found to influence MPs' abundance. The study also noted a potential correlation between atmospheric MPs and particulate matter (PM) emissions, suggesting shared sources or accumulation mechanisms. Estimates of daily MPs intake through dust ingestion highlighted associated health risks. This research provides insights into the dynamics of MPs and PM in air-conditioned offices, emphasizing the need for further investigation into their environmental and health impacts. Effective mitigation strategies are crucial for reducing MP and PM exposure, thereby improving indoor air quality and protecting human health.

Keywords: microplastics, pollution, particulate matter

eISSN 0128-2581

1. INTRODUCTION

Microplastic particles (MPs) are raising significant concern due to their potential adverse effects on human health and the environment. These particles formed through the breakdown of larger plastic objects and deliberate production for different purposes. They can vary in size, ranging from nanometers to millimeters [1]. Indoor environments, such as residences and workplaces, are especially vulnerable to contamination by microplastics (MPs) originating from sources such as synthetic fabrics and consumer goods [2]. A critical issue arises from the re-suspension of MPs into the air, complicating the situation by increasing the risk of human exposure via inhalation [3].

Current research emphasizes the need to comprehend the origins and consequences of indoor microplastic (MPs) pollution for human health and the management of indoor air quality [4]. In response to this gap, the present study aims to investigate the environmental factors that influence the resuspension of MPs and particulate matter, in indoor air. By examining these environmental conditions, such as air flow and humidity, the study seeks to provide a clearer understanding of the extent of indoor microplastic pollution and its potential health impacts. This knowledge can support efforts to mitigate exposure and improve indoor air quality management strategies. Thus, this study examines the environmental influences on atmospheric and particulate matter resuspension in the air to gain a better understanding of the extent of microplastic pollution indoors.

2. METHODOLOGY

The research aims to investigate the resuspension of microplastics (MPs) and Particulate Matter (PM) in indoor environments influenced by AC systems within the initial 0-6 hours after activation. The sampling was done at Air Resource Research Laboratory, situated on the Universiti Teknologi Malaysia Kuala Lumpur Campus. from November 2023 to March 2024. The sampling method used was passive sampling, conducted under two different conditions: with air conditioning (labeled as AC) and without air conditioning (labeled as XAC). A total of 42

samples are gathered under settings when the air conditioning system is both operational and non-operational. Each condition was subjected to a total of six-hour cycles by using six basins each cycle, in addition to one control sample for contamination control. The sampling circumstances will ensure a consistent temperature of 16 degrees Celsius, utilizing fan settings at a moderate pace. Particle counters (Model: Lighthouse Handheld 2016) were used to measure the average total particulate matter concentration. Visual identification using a Stereomicroscope (Model: Leica EZ4W) to evaluate physical attributes such as size, shape (e.g., fiber, film, foam, fragment), and color variations (e.g., transparent, black, red, blue, green, orange, yellow).

An anemometer (Model: Lutron; AM4214SD) was used to measure environmental parameters such as temperature, humidity, and air flowrate to evaluate their influence on particle resuspension. The association between atmospheric MPs and PM levels were established using comparison between abundance of MPs and particulate concentration. Meanwhile the Estimated Daily Intake (EDI) was evaluated across different age groups by using Equation 1.

$$EDI\left(\frac{particles}{kg.day}\right) = \frac{Cp \times f \times IR}{BW} \quad (1)$$

Where, Cp is the concentration of target MPs(particles/g) found in this study, f is the exposure time fraction of MPs based on age group, IR is the indoor dust ingestion rate (g/day), and BW is the average body weight of various age groups (kg). The exposure time fraction was taken based on 8 hours of working time meanwhile the IR value was taken as 0.03g/day [10] and the BW was taken as 53kg and 63kg for teenagers and adults respectively [11].

3. RESULTS AND DISCUSSION

3.1 Physical Characteristics of Indoor MPs

Figure 1 shows various shapes of MPs (A), sizes of MPs in different conditions (B), and colors of MPs (C) which consist of beads, film, fragments and fiber for both conditions. In the AC environment, beads make up the largest portion, accounting for 52% of the MPs, followed by fragments at 18%, fibers/filaments at 17%, and films at 13%. This shows that bead-shaped MPs are the most common in air-conditioned spaces, with a relatively balanced distribution among the other types of MPs. In contrast, the XAC environment shows a significantly higher proportion of beads, comprising 72% of the MPs. Fragments and fibers/filaments are both present at 18% and 6%, respectively, while films make up only 4%. This suggests that bead-shaped MPs are even more dominant in non-air-conditioned environments, while the other types of MPs, particularly films, are less prevalent. Overall, the charts indicate that air-conditioned spaces have a more varied distribution of MP types, whereas non-air-conditioned spaces tend to be dominated by beads. This difference may be due to how air circulation, temperature, and humidity in AC settings affect the fragmentation or distribution of different types of MPs. This finding is contradicted with the finding from previous study where fiber is the most common shape found in indoor environment [5]. This may be attributed to the mechanical breakdown of plastics within the air conditioning system, where air circulation through filters and ducts causes abrasion and turbulence, resulting in a higher proportion of bead-shaped MPs.

Figure 1(B) shows the percentage of MPs across four size ranges: less than 50 µm, 50–100 µm, 100–500 µm, and greater than 500 µm. The smallest MPs, those under 50 µm, dominate both environments, accounting for 54.2% in XAC and 53.9% in AC, showing a nearly identical distribution. The second largest group is MPs sized between 50 and 100 µm, making up around 26.5% and 25.4% in XAC and AC, respectively. MPs in the 100–500 µm range represent a smaller proportion, with 15.1% in XAC and 14.2% in AC. The largest MPs, those greater than 500 µm, are the least common, contributing only 6.0% in XAC and 5.3% in AC. Overall, the size distribution of MPs is similar between the two environments, with smaller MPs being the most prevalent in both. This indicates that the presence of air conditioning does not significantly alter the size range of MPs found indoors, although it may still influence their movement or suspension. The dominance of MPs smaller than 50 µm is particularly concerning, as these are more likely to be inhaled and pose potential health risks. This finding also contradict with previous study found by Sin Yee et al., (2023) and Zhang et al., (2020) [6] where the majority size falls in more than 50µm. This discrepancy may be attributed to differences in sampling methodologies, environmental conditions, or the specific office environments studied.

Furthermore, Figure 1(C) shows seven (7) different colours are present in the room, which are transparent, black, red, blue, green, orange and yellow. Transparent and black microplastics dominate both conditions, with transparent MPs accounting for approximately 42.5% and 40.1%, respectively, making them the most prevalent. Black MPs as the second most common, making up around 22.4% and 21.1% in the two sets. In both conditions, orange microplastics appear next in significance, comprising around 12.5% and 13.6%. Meanwhile, red, blue, green, and yellow microplastics are less frequent but still notable. Red MPs contribute between 6.1% and 8.0%, while blue and green MPs each range from 5.0% to 7.1%. Interestingly, yellow microplastics show a marked increase from 3.5% in the first dataset to 6.9% in the second. This prevalence is indicative of typical plastic materials commonly found in office environments, such as packaging and office supplies. The frequent occurrence of transparent MPs in this and other studies suggests the potential for these particles to be affected during organic matter removal processes, such as

acid digestion, potentially leading to their leaching or degradation [7, 5].

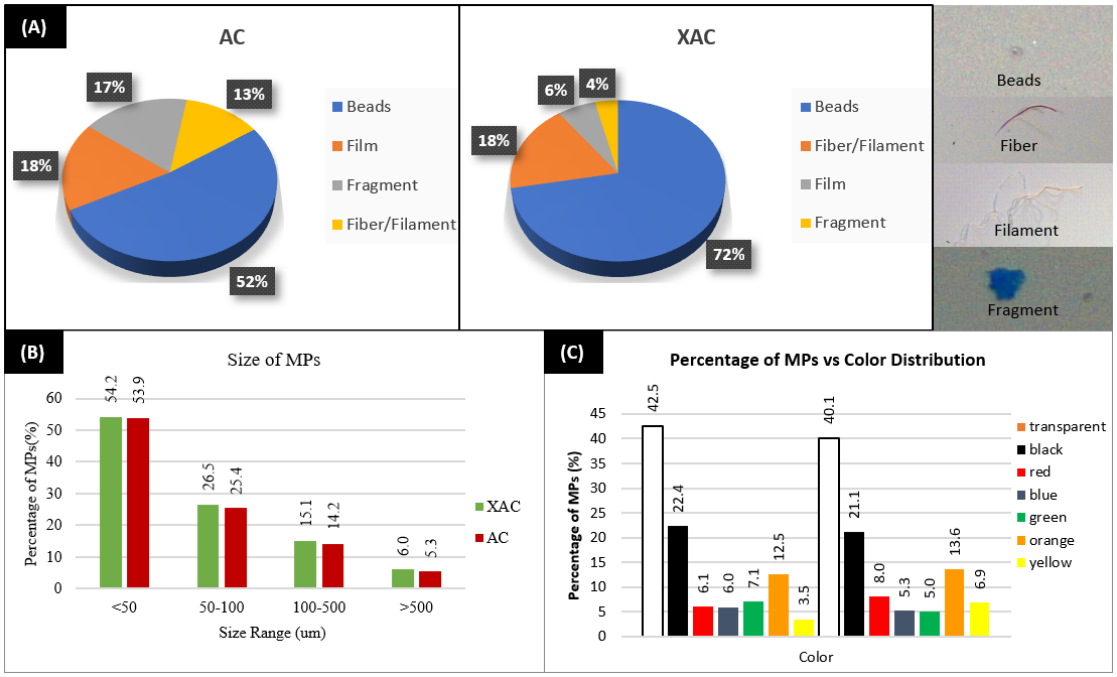

Fig. 1. Physical characteristics of indoor MPs (A) Shapes, (B) Sizes and (C) Colour

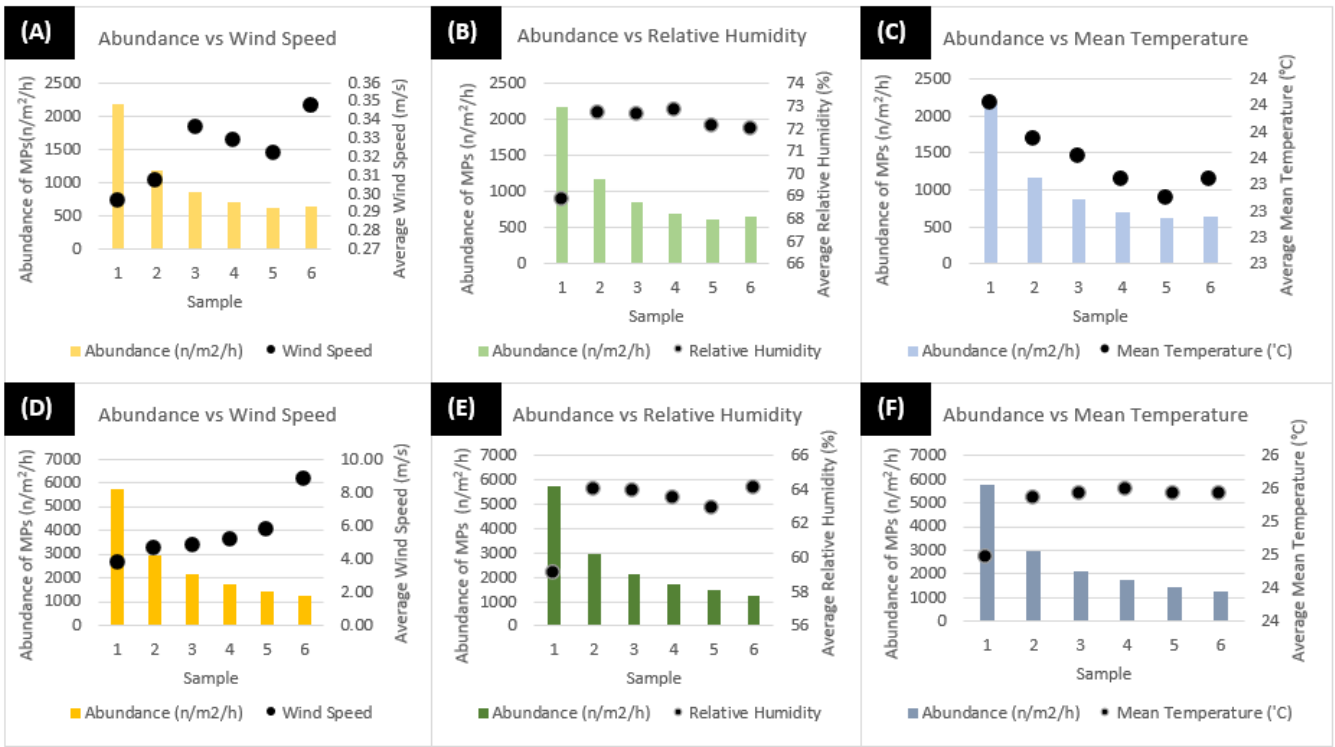

Fig. 2. Environmental Factor of MPs (A) Wind Speed with AC, (B) Relative Humidity with AC, (C) Mean Temperature with AC, (D) Wind speed without AC, (E) Relative Humidity without AC, and (F) Mean Temperature without AC.

3.2 Influence of Environmental Parameters on MPs Abundance in Air-Conditioned and Non-Air-Conditioned Environments

Figure 2 illustrates the relation of different environmental parameters on MPs abundance which shows environments. The environmental parameters include average wind speed, relative humidity, and mean temperature. The result shows that higher wind speeds correlate with decreased MP abundance, especially in air-conditioned environments. This outcome may be explained by the air circulation patterns in air-conditioned spaces, where HVAC systems could create a more controlled and consistent airflow that disperses MPs more effectively, reducing their localized concentration.

Meanwhile, Figure 2(B and E) indicates that higher relative humidity levels are linked to greater MP presence, likely because elevated humidity can influence particle behavior, such as by enhancing their suspension or reducing adhesion to surfaces. Previous study has shown that environmental parameters such as wind speed and humidity play significant roles in the distribution and transport of MPs in the atmosphere [8]. This study discussed how higher wind speeds could lead to the dispersion of MPs, while elevated humidity levels might enhance their suspension or reduce adhesion to surfaces, which aligns with the findings of the current study.

3.3 Comparison of MPs Abundances and Particulate Matter Concentration in Air-Conditioned and Non-Air-Conditioned Environments

Figure 3(A) shows six charts comparing the abundance of MPs under different environmental conditions, both with and without AC. Each chart depicts how MP abundance (n/m²/h) correlates with a specific environmental factor such as wind speed, relative humidity, or mean temperature. The black dots in each chart represent the average values of the environmental factor, while the bars represent the MP abundance. Without AC, MPs initially deposited at a rate of 5736.7 n/m²/h in the first hour, decreasing to 1261.7 n/m²/h by the sixth hour. This decline suggests factors like reduced air turbulence and decreased shedding from office materials and occupants. In contrast, with AC, deposition rates were lower, starting at 2174.2 n/m²/h and decreasing to 648.3 n/m²/h by the sixth hour, indicating improved air circulation and reduced particle settling. Thus, the findings highlight that AC systems play a critical role in managing indoor MPs pollution by maintaining lower and more consistent deposition rates compared to non-AC environments.

According to Figure 3(B and C), with the air conditioner running, PM concentrations ranged from 18 to 25 µg/m³, correlating with MPs abundance ranging from 620.8 to 2174.2 n/m²/h. Without the air conditioner, PM levels varied between 26 and 32 µg/m³, alongside MPs abundance ranging from 1261.7 to 5736.7 n/m²/h. These results suggest a positive correlation between higher PM concentrations and increased MPs abundance, particularly noticeable in non-airconditioned settings which is agreeable with previous study [9].

In the presence of AC, the relationship between environmental factors and MP abundance appears more moderate. For example, wind speed (Chart A) shows a slight variation, and MP abundance generally decreases across the samples. Similarly, relative humidity (Chart B) reveals no clear trend, indicating that higher humidity levels under AC conditions do not significantly impact MP abundance. Meanwhile, mean temperature (Chart C) demonstrates a slight decline in both temperature and MP abundance, suggesting a more stable environment when AC is used.

In contrast, without AC, the environmental factors have a more pronounced effect on MP abundance. Wind speed (Chart D) shows a strong positive correlation, where higher wind speeds are associated with a significant increase in MP abundance. For relative humidity (Chart E), there is an inverse relationship, where higher humidity levels lead to a marked decrease in MP abundance. Finally, the mean temperature (Chart F) without AC shows a more substantial decrease in both temperature and MP abundance, with MP levels being notably higher compared to the AC scenario.

Overall, the figure highlights that air conditioning plays a moderating role in mitigating the impact of environmental factors such as wind speed and temperature on microplastic abundance, while conditions without AC lead to greater fluctuations in MP levels.

Previous study suggested that PM2.5 and MPs could potentially serve as carriers for airborne MPs and polycyclic aromatic hydrocarbons (PAHs). The study implies shared emission sources or accumulation mechanisms affecting both PM and MPs in ambient air. Additionally, the findings suggest that air conditioner usage may influence this relationship, potentially reducing the buildup of both pollutants.

3.4 Comparison of MPs Estimated Daily Intake in Air-Conditioned and Non-Air-Conditioned Environments

The results shown in Table 1 are a comparison of the estimated daily intake (EDI) of MPs in particles per kilogram per day for teenagers and adults under two different conditions: with and without AC. For teenagers, the EDI of MPs is 0.42 particles/kg/day when AC is used, which increases to 0.88 particles/kg/day without AC. Similarly, for adults, the EDI is lower with AC at 0.25 particles/kg/day, but it rises to 0.53 particles/kg/day in the absence of AC.

Teenagers routinely exhibit elevated consumption rates compared to adults, irrespective of the presence of air conditioning, potentially because of disparities in activity levels or respiration rates. It also emphasizes that teenagers are more susceptible to greater amounts of MPs consumption compared to adults.

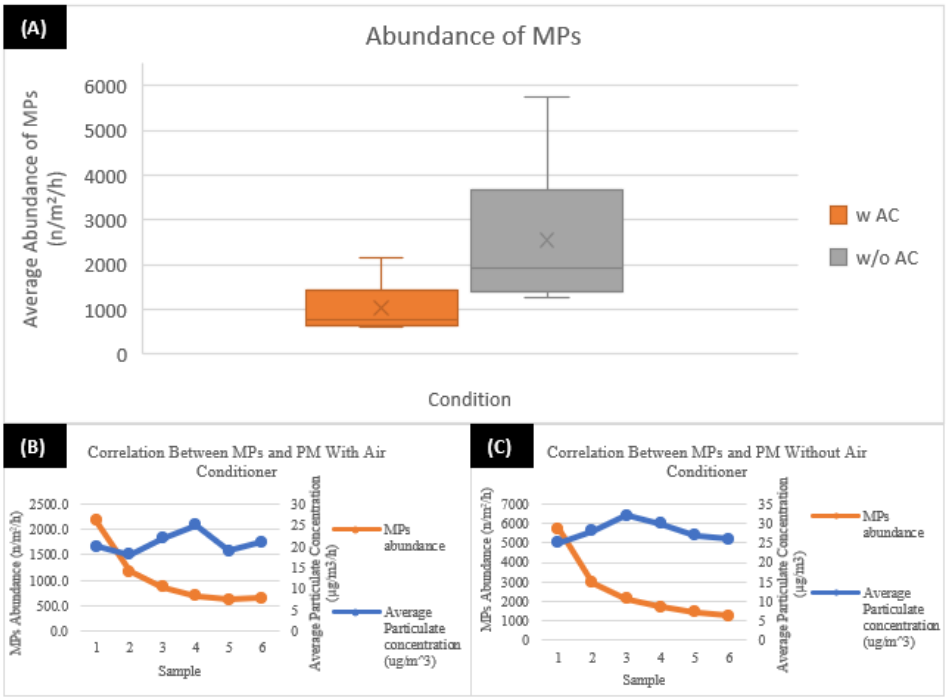

Fig. 3. Comparative Analysis (A) Abundance of MPs, Correlation Between MPs and PM (B) with Air Conditioner and (C) without Air Conditioner.

Table 1. EDI Comparison for Various Age Under Different Conditions

Conditions	Estimated daily intake of MPs (particle/kg.day)	
	Teenagers	Adults
With Air Conditioning	0.42	0.25
Without Air Conditioning	0.88	0.53

4. CONCLUSION

The study underscores the significant impacts of air conditioning on indoor MPs distribution and characteristics. AC environments show higher proportions of bead-shaped MPs, indicating potential fragmentation influenced by consistent temperatures and humidity levels. Both AC and non-AC settings feature MPs smaller than 50µm as predominant, raising concerns for respiratory health impacts upon inhalation. Transparent and black MPs dominate in both environments, with AC systems contributing to higher MP suspension rates due to increased wind speed and humidity. AC also reduces MPs accumulation on indoor surfaces, suggesting a complex interplay between AC use, indoor air quality, and potential health implications that warrant further investigation and management strategies. Future work should also investigate AC filtration systems to reduce indoor MPs concentrations.

ACKNOWLEDGEMENTS

The authors would like to acknowledge the financial support from Universiti Teknologi Malaysia under the final-year project and through Universiti Teknologi Malaysia Fundamental Research (UTMFR) Grant project no. Q.K130000.3843.23H40 and Fundamental Research Grant Scheme (FRGS) under a grant number of FRGS/1/2022/TK05/UTM/02/46 from the Ministry of Higher Education Malaysia.

REFERENCES

[1] Y. Yao, M. Glamoclija, A. Murphy, and Y. Gao (2022). doi: 10.1016/j.envres.2021.112142.

[2] S. Kacprzak and L. D. Tijing, (2022) 107359.
[3] A. Torres-Agullo, A. Karanasiou, T. Moreno, and S. Lacorte, (2021) 149555. doi: 10.1016/j.scitotenv.2021.149555.
[4] M. Dewika et al., (2023) 324. doi: 10.1016/j.chemosphere.2023.138270.
[5] Sin Yee, C., Yasina Yusuf, S., Mohd Noor, S., Ruwaida Jamian, N., Ramli, N., Naidu, D., & Monica, M. (2023). 01004. https://doi.org/10.1051/e3sconf/202343701004
[6] Zhang, Y., Kang, S., Allen, S., Allen, D., Gao, T., & Sillanpää, M. (2020). 103118. https://doi.org/10.1016/j.earscirev.2020.103118
[7] Sheraz, M., Kim, J., & Kim, J. (2023). 274–304. https://doi.org/10.1016/j.psep.2023.10.002
[8] Mukai, C., Siegel, J. A., & Novoselac, A. (2009). 1022–1032. https://doi.org/10.1080/02786820903131073
[9] Akhbarizadeh, R., Dobaradaran, S., Amouei Torkmahalleh, M., Saeedi, R., Aibaghi, R., & Faraji Ghasemi, F. (2021) 110339. https://doi.org/10.1016/j.envres.2020.110339
[10] Us Epa, U. (2011).
[11] Liao, C., Liu, F., Guo, Y., Moon, H. B., Nakata, H., Wu, Q., et al. (2012). 9138–9145. doi:10.1021/es302004w.

Malaysian Journal of Catalysis
http://mjcat.utm.my/
MJCat Research Article

Characterization and Performance Test of Sulfonated Activated Carbon as a Catalyst in the Levulinic Acid Production Process from Cellulose

Didi Dwi Anggoro[1], Istadi[1], Luqman Buchori[1], Setia Budi Sasongko[1], Novita Susanto[1], Safira Febe Wijaya[1], Brilliant Umara Le Monde[1]

[1]*Department of Chemical Engineering, Faculty of Engineering, Diponegoro University, Jl. Prof. H. Soedarto S.H., Semarang 50275, Indonesia*

**Corresponding Author: dd_anggoro@che.undip.ac.id*

Article history:
Received 02 October 2024
Accepted 23 December 2024

ABSTRACT

The production levulinic acid from cellulose was investigated using activated carbon as catalyst. This research conducted the characterize of activated carbon, sulfonated activated carbon, and nickel impregnation into sulfonated activated carbon. The results showed that the acidity of the activated carbon catalyst is 1233.046 µmol/g, while the Ni/sulfonated activated carbon had the highest catalyst acidity of 6106.512 µmol/g. In addition, the highest acidity of the sulfonated activated carbon catalyst was obtained at a sulfonation temperature variable of 150℃ and a H_2SO_4 concentration of 10 N is 5108.332 µmol/g. The results of FTIR analysis show that in the sulfonated activated carbon catalyst, the S-O, S=O, and C-S groups appear at wavelengths of 748-883 cm^{-1}, 1148 cm^{-1}, and around 600 cm^{-1} respectively, which proves that the sulfonic acid group successfully attached to the surface of the sulfonated carbon catalyst. Meanwhile in Ni/sulfonated activated carbon, the Ni^{2+} peak appears at a wavelength of 473 cm^{-1}. XRD patterns of the three variables, indicating that sulfonation does not affect the carbon microstructure. The appearance of a new peak at 43° indicates the presence of NiO species in Ni/sulfonated activated carbon and the sharper peaks in Ni/sulfonated activated carbon indicate that there has been a change in the amorphous area to crystalline. Catalyst performance test show that hydrothermal cellulose without catalyst produces a cellulose conversion of 12% and levulinic acid yield of 1.12% while activated carbon catalyst produces a cellulose conversion of 20% and levulinic acid yield of 1.26%. The results of the catalyst performance test also show that hydrothermal cellulose using sulfonated activated carbon produces a conversion of 30% and levulinic acid yield of 3.95% due to the presence of -COOH, -OH, and $-SO_3H$ functional groups. The highest cellulose conversion of 42% and levulinic acid yield of 4.47% were achieved when using Ni/sulfonated activated carbon.

Keywords: *SAC, hydrothermal, cellulose, levulinic acid, catalyst*

| eISSN 0128-2581 |

1. INTRODUCTION

Biofuel and biochemical production from biomass have the potential to reduce dependence on traditional fossil fuels, reduce greenhouse gases, and increase energy security [1]. Levulinic acid has been identified as one of the most important value-added chemicals derived from biomass. The two functional groups of levulinic acid, namely ketone and carboxylic acid, make it important as a raw material for the production of various biomass-derived commodities [2]. Levulinic acid is known as a platform chemical because it can produce various other compounds, such as 5-bromolevulinic acid, valeric acid, MTHF, methyl pyrrolidone, and others. The potential of levulinic acid as a biofuel is very large because levulinic acid can be converted into γ-valerolactone (GVL), 2-methyltetrahydrofuran, and levulinate esters where these three products are alternative fuels to replace fossil fuels [3]. In addition, levulinic acid can also be used as an additive in the production of cosmetics, plastics, and textiles [4]. Initially, sugars and starches extracted from agricultural crops were highly desirable raw materials for biochemical production. However, this has caused controversy with food producers [5]. Glucose produced from the hydrolysis of cellulose in lignocellulose is an important platform that can be converted into valuable chemicals (e.g. furfural, 5-hydroxymethylfurfural, levulinic acid) and renewable biofuels (e.g. bioethanol, biobutanol, and hydrocarbons) [6]. Several technologies, such as direct combustion, pyrolysis, hydrolysis, and hydrothermal conversion (HTC), have been developed to convert biomass into valuable fuels or chemicals. Among these methods, hydrothermal is a promising method because it can be applied to wet biomass, has a lower temperature than pyrolysis, and has high energy efficiency [7]. During the hydrothermal process, water acts as a reactant and catalyst. In particular, exposure to water at high temperatures and pressures can cause the cellulose crystal structure to become amorphous [8].

In general, the biomass hydrothermal method using an acid catalyst is one of the processes that can be carried out to produce levulinic acid. Consecutively, the cellulose fraction in the biomass will be converted into glucose, then glucose will be dehydrated into hydroxymethylfurfural (HMF) and HMF will undergo rehydration with the help of two water molecules to produce levulinic acid [3]. Glucose can be produced from cellulose by breaking the β-1,4-glycosidic bond between glucose units through hydrolysis catalyzed by acid or enzymes (cellulase). However, currently cellulase is expensive to produce and difficult to recycle. In addition, enzymatic hydrolysis also requires initial processing of lignocellulosic biomass which consumes a lot of energy and costs to produce satisfactory glucose [6]. Meanwhile, reactions with acid catalysts are very important in chemical processes. Acid catalysts have been studied and developed over the past few decades. Homogeneous acid catalysts, such as H_2SO_4, HF, HNO_3, and H_3PO_4 are widely used as homogeneous acid catalyst fluids that show effective catalytic performance even at low temperatures [9]. However, homogeneous acid catalysts cause several problems such as strong protonic acid catalysts easily corrode production equipment during the reaction process, are difficult to separate and recycle if mixed with products after the reaction, and produce acid waste that pollutes the environment [10]. Along with the excitement of green and sustainable development, the application of homogeneous acid catalysts is becoming less popular and is starting to be replaced by the use of heterogeneous catalysts.

To overcome these problems, solid acid catalysts have been gradually developed such as magnetic solid acid catalysts, sulfonated zirconia, sulfonated activated carbon, Amberlyst-15, zeolites, and so on. Among various types of heterogeneous solid catalysts, carbon-based solid acid catalysts show superior catalytic activity [11]. This is due to the high acid density, good thermodynamic stability, excellent surface hydrophobicity, and high chemical stability. In addition, carbon-based solid catalysts can be prepared using cheap and renewable biomass raw materials and their derivatives, thereby reducing production costs [12]. Biomass waste has been used as a carbon precursor for the manufacture of solid acid catalysts such as activated carbon catalysts through carbonization and activation processes. Due to the low catalytic performance of activated carbon for the hydrolysis of cellulose into simple sugars, a sulfonation process is required. Sulfonation is the process of attaching sulfonate groups ($–SO_3H$) to the surface of activated carbon. This process aims to increase acidity and catalytic activity. The sulfonation process is easy to do, cheap, and can be applied in various solid catalysts [13]. Sulfonated activated carbon catalysts have a stable carbon framework and are insoluble in most acidic/basic conditions and organic solvents. In addition, this catalyst can also be separated from the reaction system so that it is easy to recover and reuse [9].

To increase the effectiveness and selectivity of the catalyst, many active sites are needed in sulfonated activated carbon so that the catalytic activity will increase [14]. Acid sites on sulfonated activated carbon can be increased using metal development by impregnation. In addition to producing little waste, the impregnation process is easy to do and has a high success rate [15]. One of the most effective metals used is nickel metal [14]. Ni metal has a low price and has been proven to have good catalytic activity because it has an empty d orbital so that it can increase the acidity of the sulfonated activated carbon catalyst [16]. Therefore, the use of solid acid catalysts based on sulfonated activated carbon impregnated with nickel metal which is easily separated so that the catalyst can be recovered and reused also provides high catalytic activity and selectivity, has been developed.

In this study, the synthesis of sulfonated activated carbon catalysts and sulfonated activated carbon with nickel impregnation will be carried out. Furthermore, the catalysts were characterized and tested for acidity by studying the effect of reaction temperature and H_2SO_4 concentration on the sulfonation process of activated carbon. In addition, the performance of sulfonated activated carbon catalysts and sulfonated activated carbon catalysts impregnated with nickel metal for the production of levulinic acid from cellulose will also be studied.

2. EXPERIMENTS

2.1 Materials

The materials used in this work were activated carbon, sulfuric acid (H_2SO_4, 98%, EMSURE, Merck), cellulose (Aldrich), inert nitrogen gas (N_2) (Aneka Gas), and nickel (II) sulfate hexahydrate ($NiSO_4.6H_2O$, EMSURE, Merck).

2.2 Synthesis of Sulfonated Activated Carbon

Activated carbon is sulfonated by mixing 10 grams of 80 mesh activated carbon into 150 mL of H_2SO_4 solution in various concentrations. Then stirred with a magnetic stirrer and hotplate at a certain temperature for 4 hours. Next, the mixture resulting from the sulfonation process is filtered using Whatman filter paper while washing with distilled water to obtain the sulfonated activated carbon catalyst. After that, the catalyst drying process is carried out in an oven with the aim of removing the remaining distilled water from the washing process. The drying process takes place in an oven at a temperature of 110°C.

2.3 Sulfonated Activated Carbon Acidity Test

The acidity test of the sulfonated activated carbon catalyst was carried out quantitatively using the gravimetric method and ammonia as the adsorbate base. Ammonia gas molecules will diffuse into the sulfonated activated carbon pores and be adsorbed at active sites on the surface. Ammonia adsorption on the sulfonated activated carbon surface can occur physically and chemically. Ammonia is physically adsorbed to the sulfonated activated carbon surface via weak van der Waals forces and chemically

adsorbed to the sulfonated activated carbon surface via strong hydrogen bonds. Hydrogen bonds occur between hydrogen atoms of ammonia and oxygen atoms of hydroxyl/carboxyl groups on the surface of sulfonated activated carbon [17]. This method is carried out by placing 1 gram of the catalyst sample in a cup, then placing it in a desiccator which has previously been saturated with ammonia vapor, and leaving it for 24 hours. The acidity level of the catalyst can be calculated using the following equation [18].

$$\text{Ammonia adsorption (mmol/g)} = \left(\frac{W_2 - W_1}{W_1 - W_0} \times \frac{1}{Mr}\right) \times \frac{1000\ \text{mmol}}{\text{mol}} \quad (2.1)$$

where:
W_0 = weight of empty cup (g)
W_1 = weight of cup + sample before treatment (g)
W_2 = weight of cup + sample after treatment (g)
Mr = molecular weight of ammonia (g/mol)

2.4 Synthesis of Nickel/Sulfonated Activated Carbon

Sulfonated activated carbon with the highest acidity level is then impregnated with nickel. 5 grams of activated carbon was added to nickel metal contained in a hexahydrate sulfate salt solution ($NiSO_4.6H_2O$) with a concentration of 2.5% wt and dissolved in 20 mL of distilled water. Then cover the mixture with aluminum foil while stirring with a magnetic stirrer at 80°C for 3 hours. Next, the mixture resulting from the impregnation process was filtered using Whatman filter paper while washed with distilled water to obtain the Ni/SAC catalyst and dried in an oven at 105°C for 24 hours. The sulfonated activated carbon impregnated with oven-dried nickel metal is then calcined at a temperature of 400°C for 2 hours.

2.5 Catalyst Characterization

Fourier Transform Infrared (FTIR) analysis aims to determine the functional groups of activated carbon before sulfonation (AC), after sulfonation (SAC), and sulfonated activated carbon after nickel metal impregnation (Ni/SAC). This analysis was carried out at the Physics Laboratory of Negeri Semarang University with a Perkin-Elmer Spotlight 200 at a spectrum range of 400-4000 cm^{-1}. XRD characterization was used with the aim of determining the structure and identification of crystals (crystallinity) in AC, SAC, and Ni/SAC which was carried out at the Physics Laboratory of Negeri Semarang University using Panalytical X'Pert 3 Powder. The crystallinity of the catalyst can be calculated using the following equation:

$$\text{Crystallinity} = \frac{\text{crystalline peak area}}{\text{overall peak area (amorf and crystalline)}} \times 100\% \quad (2.2)$$

2.6 Production of Levulinic Acid

AC, SAC, and Ni/SAC were used as catalysts in the hydrothermal production process of levulinic acid from cellulose using a 100 mL autoclave reactor. The reactor was filled with 1 gram of cellulose, 12%wt catalyst each, and the volume was adjusted to 60 mL by adding deionized water as a solvent. Then the reactor was injected with inert gas in the form of nitrogen gas (N_2) to remove air in the autoclave. The reactor was heated to the desired reaction temperature of 150°C. When the specified conditions were reached, the reaction was calculated to start for a reaction time of 2.5 hours. After the reaction was complete, the heater was turned off. The reaction mixture was filtered to separate liquid and solid products. The filtrate was analyzed to determine the level of levulinic acid produced using HPLC (High Performance Liquid Chromatography) (Perkin-Elmer Altus). While the remaining cellulose after hydrothermal was dried in an oven at a temperature of 110°C until its weight was constant and then calculated the cellulose conversion with the following equation [19].

$$\text{Conversion of cellulose (\%)} = \frac{\text{initial cellulose weight (g)} - \text{cellulose weight after hydrothermal (g)}}{\text{initial cellulose (g)}} \times 100\% \quad (2.3)$$

3. RESULTS AND DISCUSSION

3.1 Effect of Sulfonation Temperature on Total Acidity of Sulfonated Activated Carbon Catalyst

One of the factors that affect the total acidity of sulfonated activated carbon catalyst is the sulfonation temperature. In this study, the sulfonation reaction was carried out with 6 N, 8 N, and 10 N H_2SO_4 solutions and stirring at temperatures of 120°C, 150°C, and 180°C. The effect of sulfonation temperature on the total acidity of sulfonated activated carbon catalyst is shown in Fig 1.

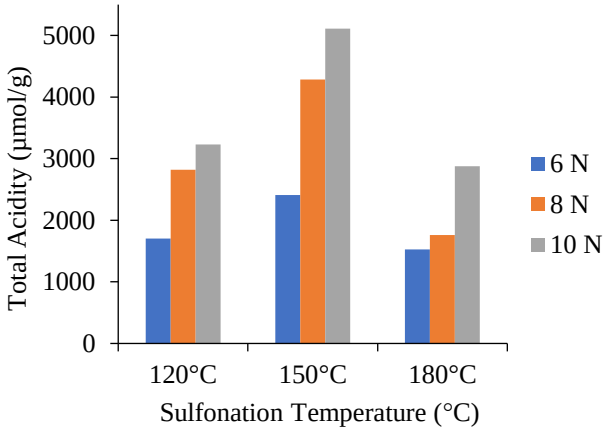

Fig. 1. Effect of sulfonation temperature on the total acidity of the catalyst

Based on Fig 1, it can be seen that the effect of sulfonation temperature on the total acidity of the sulfonated activated carbon produced is fluctuating. At a sulfonation temperature of 120 ºC, the total acidity obtained at H_2SO_4 concentrations of 6 N, 8 N, and 10 N were respectively 1702.777 µmol/g; 2818.390 µmol/g; and 3229.405 µmol/g. At a sulfonation temperature of 150 ºC, the total acidity obtained at H_2SO_4 concentrations of 6 N, 8 N, and 10 N were respectively 2407.375 µmol/g; 4286.301 µmol/g; and 5108.332 µmol/g. Meanwhile, at a sulfonation temperature of 180 ºC, the total acidity obtained at H_2SO_4 concentrations of 6 N, 8 N, and 10 N were respectively 1526.628 µmol/g; 1761.494 µmol/g; and 2877.106 µmol/g. This shows that the highest total acidity was obtained at a sulfonation temperature of 150 ºC with a H_2SO_4 concentration of 10N.

When the sulfonation temperature increases, the acidity of the sulfonated activated carbon catalyst produced will also increase. However, at a sulfonation temperature that is too high, the acidity value of the catalyst decreases. The high temperature applied during the sulfonation process causes the stability of organic molecules to decrease and eventually causes the separation of intermolecular bonds [20]. The acidity of the sulfonated activated carbon catalyst can be measured from the adsorption results on ammonia bases which are linearly correlated with the number of active sites in the catalyst and its catalytic activity. The increase in ammonia adsorption on sulfonated activated carbon indicates that the pores and active sites of the catalyst are increasingly open so that the ammonia adsorption process by sulfonated activated carbon is more optimal [21]. The acidity of all catalysts produced is related to the SO_3H acid sites associated with the oxidation of functional groups such as -OH groups in the catalyst structure. The total acidity of the catalyst is largely influenced by the oxidation of the -OH functional groups on the surface of activated carbon which produces additional carboxyl sites (oxygen functional groups) [22]. At too high sulfonation temperatures, degradation of the -OH functional groups occur so that the acidity of the catalyst decreases. The higher the temperature during the preparation of activated carbon, the lower the amount of hydrogen and oxygen content which is thought to be the main factor in reducing the -OH functional groups [23]. In addition, if the sulfonation temperature is too high, it can damage the pore structure of activated carbon so that the number of active sites decreases and the total acidity of the catalyst decreases [6].

3.2 Effect of H_2SO_4 Concentration on Total Acidity of Sulfonated Activated Carbon Catalyst

Another factor that affects the total acidity of sulfonated activated carbon catalyst is the concentration of sulfuric acid. In this study, the sulfonation reaction was carried out with 6 N, 8 N, and 10 N H_2SO_4 solutions and stirring at temperatures of 120ºC, 150ºC, and 180ºC. The effect of H_2SO_4 concentration on the total acidity of sulfonated activated carbon catalyst is shown in Fig 2.

Based on Fig 2, it can be seen that the effect of H_2SO_4 concentration is directly proportional to the total acidity of the sulfonated activated carbon produced. At a concentration of H_2SO_4 6 N, the total acidity obtained at sulfonation temperatures of 120 ºC, 150 ºC, and 180 ºC were respectively 1702.777 µmol/g; 2407.375 µmol/g; and 1526.628 µmol/g. At a concentration of H_2SO_4 8 N, the total acidity obtained at sulfonation temperatures of 120 ºC, 150 ºC, and 180 ºC were respectively 2818.390 µmol/g; 4286.301 µmol/g; and 1761.494 µmol/g. Meanwhile, at a concentration of 10 N H_2SO_4, the total acidity obtained at sulfonation temperatures of 120 ºC, 150 ºC, and 180 ºC were respectively 3229.405 µmol/g; 5108.332 µmol/g; and 2877.106 µmol/g. This shows that the highest total acidity was obtained at a concentration of 10 N H_2SO_4 with a sulfonation temperature of 150 ºC.

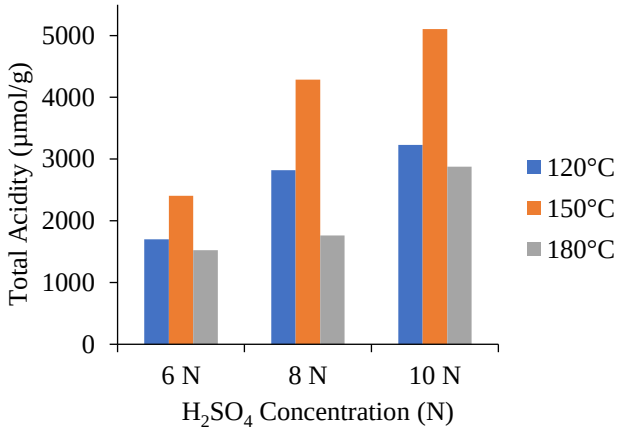

Fig. 2. Effect of H_2SO_4 concentration on the total acidity of the catalyst

The concentration of H_2SO_4 affects the total acidity of sulfonated activated carbon produced from the sulfonation process of activated carbon. The greater the concentration of H_2SO_4 as a sulfonation precursor, the greater the total acidity of the sulfonated activated carbon catalyst. The sulfonation process on activated carbon causes sulfonate groups ($-SO_3H$) to be adsorbed on the pores of the activated carbon. The increasing number of acid sites in the form of adsorbed sulfonate groups will increase the acidity of the activated carbon catalyst [24]. The acidity of the sulfonated activated carbon catalyst tends to increase with the increasing concentration of sulfuric acid as a sulfonation precursor, which means that more sulfonate groups are bound to the surface of the activated carbon. The high acidity of this sulfonated activated carbon catalyst can accelerate the hydrolysis of cellulose into glucose or simple sugars [13]. The acidity of sulfonated activated carbon can be seen from the adsorption results against ammonia base where the increase in acidity occurs due to the more optimal ammonia adsorption process because the catalyst pores are more open [25].

3.3 Catalyst Characterization

3.3.1 Fourier Transform Infrared (FTIR) Analysis

In this study, the FTIR test was used to observe changes in the functional groups of activated carbon before sulfonation (AC), after sulfonation (SAC), and sulfonated activated carbon after nickel metal impregnation (Ni/SAC) which are presented in Fig 3.

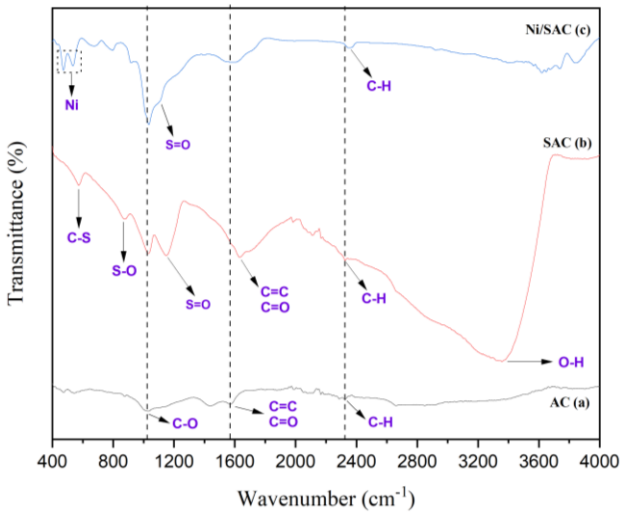

Fig. 3. FTIR spectrum of (a) AC, (b) SAC, and (c) Ni/SAC

Based on Fig 3, in AC, a peak can be seen at 1045 cm^{-1} which indicates the stretching of the C-O group [26]. Absorption at 1593 cm^{-1} indicates the stretching of the C=C and C=O groups while the wavelength of 2366 cm^{-1} indicates the stretching of the C-H aldehyde group [27]. The spectrum in SAC is similar to AC which shows that sulfonation does not change the structure of activated carbon as a catalyst support. In SAC, the stretching of the S-O group appears in the range of 748-883 cm^{-1} [11]. In addition, there is also a peak at 1148 cm^{-1} which is the stretching of the S=O group. The stretching of the C=C and C=O groups of the carbonyl and carboxylate groups is seen to shift at a wavelength of 1647 cm^{-1} and a wavelength of 3290 cm^{-1} refers to the −OH group. The remaining stretching of around 600 cm^{-1} is due to the presence of C–S binding. These results prove that the sulfonic acid group has successfully attached to the surface of the sulfonated carbon catalyst. The sharper C=O group on SAC is due to the oxidation of the -OH functional group on the AC surface which produces additional carboxyl sites [22]. In addition, the C-O peak at a wavelength of 1034 cm^{-1} also looks sharper due to the formation of new C-O bonds such as ether, phenol, and hydroxyl groups [27].

In Figure 3, it can also be seen that the Ni^{2+} peak on Ni/SAC appears at a wavelength of 473 cm^{-1}. This is in accordance with research conducted by [28] which stated that AC-Ni shows its peak around a wavelength of 400–500 cm^{-1} due to stretching of the NiO bond because most metal oxides show this bond in the absorption band between 400 cm^{-1} or 1000 cm^{-1}. However, nickel impregnation into porous activated carbon also causes changes in most functional groups, as seen from the low intensity of the bands that appear on Ni/SAC such as the -SO_3H group. This is because the temperature and impregnation time affect the prepared samples [27].

3.3.2 X-Ray Diffraction (XRD) Analysis

X-Ray Diffraction (XRD) analysis aims to determine the changes in structure and crystallinity that occur in activated carbon (AC), sulfonated activated carbon (SAC), and nickel-impregnated sulfonated activated carbon (Ni/SAC) as presented in Fig 4.

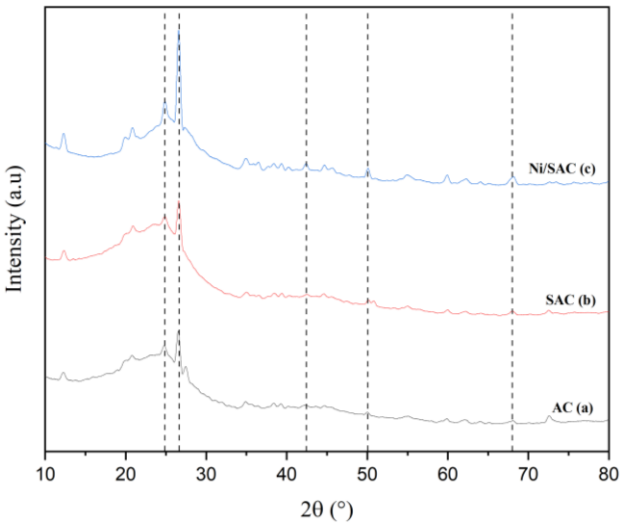

Fig. 4. XRD patterns of (a) AC, (b) SAC, and (c) Ni/SAC

Fig 4 shows the XRD patterns of activated carbon (AC), sulfonated activated carbon catalyst (SAC), and nickel-impregnated sulfonated activated carbon catalyst (Ni/SAC). The crystallinity region is depicted as a narrow and sharp peak capture while the area with a widened peak is an amorphous region [14]. The diffraction peak (2θ) 26.5º shows amorphous carbon consisting of aromatic carbon oriented in a very irregular shape. The diffraction peak (2θ) 24.8° shows a structure between graphite and amorphous carbon which also has an irregular layer [29]. Overall, there is no significant difference in the XRD pattern between activated carbon, sulfonated carbon catalyst, and nickel-impregnated sulfonated activated carbon catalyst indicating that sulfonation does not affect the microstructure of carbon. The emergence of a new peak at 43° indicates the presence of NiO species in Ni/SAC [30]. The increase in peak intensity or increasingly sharp peaks in Ni/SAC indicates that there has been a change from the amorphous region to the crystalline region, which proves that Ni metal is not only attached to the surface of activated carbon, but Ni has entered the structure of activated carbon [14].

Crystallinity can be determined by comparing the intensity or area of one (or a number of) crystalline peaks of a sample with the intensity or area of the entire peak consisting of amorphous and crystalline. Based on the calculation results using Equation 2.2, the crystallinity

values of AC, SAC, and Ni/SAC were respectively 46.0989%; 47.3293%; and 66.6073%. According to [31], the increasing crystallinity value means that the carbon structure is more regular and stronger and the better the catalyst synthesis produced. In addition, high crystallinity also indicates that the catalyst has good thermal stability [32].

3.3.3 Catalyst Performance Test for Levulinic Acid Production from Cellulose

Catalyst performance test was conducted to determine the potential of catalyst in the production of levulinic acid from cellulose. The hydrothermal process of cellulose into levulinic acid was carried out by a process without a catalyst, using activated carbon (AC), sulfonated activated carbon (SAC), and nickel-impregnated sulfonated activated carbon (Ni/SAC) catalysts. The amount of cellulose conversion and levulinic acid yield in each variable is presented in Table 1.

Table 1. Cellulose conversion and levulinic acid yield in hydrothermal processes with various catalyst variables

Variable	Cellulose Conversion (%)	Levulinic Acid Yield (%)
Without catalyst	12	1.12
Activated Carbon (AC)	20	1.26
Sulfonated Activated Carbon (SAC)	30	3.95
Nickel Impregnated Sulfonated Activated Carbon (Ni/SAC)	42	4.47

Table 1 shows that the hydrothermal process of cellulose without the use of a catalyst produces the smallest conversion of 12%. Then the conversion increases to 20% when an activated carbon (AC) catalyst is used. In sulfonated activated carbon (SAC), the conversion of cellulose increases to 30% and the highest conversion of 42% is obtained when the hydrothermal process is carried out using a sulfonated activated carbon catalyst impregnated with nickel metal (Ni/SAC).

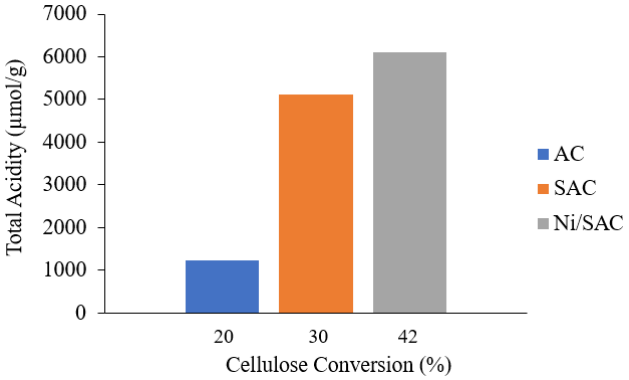

Fig. 5. Effect of total acidity of catalyst on cellulose conversion

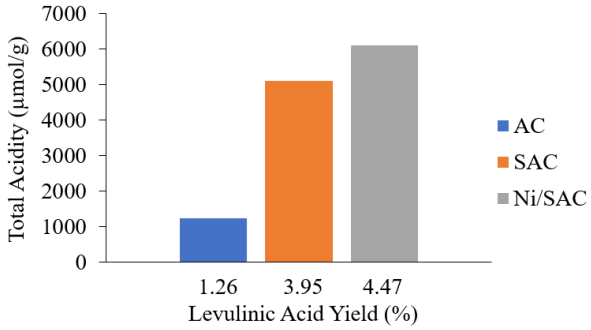

Fig. 6. Effect of total acidity of catalyst on levulinic acid yield

Based on the HPLC results in the standard solution, it can be seen that the peak of levulinic acid appears at a retention time of 9.702. Meanwhile in the other hydrothermal process without a catalyst, using an activated carbon catalyst (AC), sulfonated activated carbon (SAC), and sulfonated activated carbon impregnated with nickel (Ni/SAC), peaks of levulinic acid appears at retention time 9.071, 9.471, 9.189, and 9.058. By using data area of the HPLC results, yield of levulinic acid can be obtained in variables without catalyst, using AC, SAC, and Ni/SAC catalysts respectively at 1.12%, 1.26%, 3.95%, and 4.47%.

Acidity and SO_3H groups affect the activity of the catalyst and the resulting products where the performance of the catalyst is increased along with the increasing acidity value [11]. Fig 5 and Fig 6 show that the conversion of cellulose increases along with the increasing acidity value of AC, SAC, and Ni/SAC which are respectively 1233,046 µmol/g; 5108,332 µmol/g; and 6106,512 µmol/g. The sulfonation process plays an important role in providing SO_3H groups so that sulfonated activated carbon catalysts contain efficient -COOH, -OH, and -SO_3H functional groups for cellulose hydrolysis reactions. The presence of -OH and -COOH functional groups serves to attract the feed compound, namely cellulose, to be closer to the -SO_3H group which acts as a catalytic active site where the α-1,4 and β-1,4 glycosidic bonds of the adsorbed cellulose molecules occur in the hydrolysis process [21]. The -SO_3H group will increase the reactivity of cellulose by protonation so that it will facilitate the breaking of glycosidic bonds in cellulose, thereby increasing cellulose conversion. High total acidity will also increase the accessibility of reactants to active sites on the catalyst surface and provide a better environment for the reaction to take place [33].

The increase in cellulose conversion on the Ni/SAC catalyst is related to the increase in acidity formed by Ni metal bound to the sulfonate group (-SO_3H) thereby increasing catalytic activity [34]. In the production of levulinic acid, cellulose is first decomposed into glucose through a hydrolysis reaction. Then the simple sugar is converted into 5-HMF through dehydration and followed by a rehydration reaction into levulinic acid products. However, due to the difficulty of direct dehydration of glucose into 5-HMF, glucose needs to be isomerized first into fructose [35]. Nickel plays a role in the isomerization process of glucose

into fructose which contributes to the formation of levulinic acid [36]. The hydrolysis process of cellulose acid into glucose occurs in the sulfonate group. While the isomerization reaction is catalyzed by nickel metal where glucose is converted into fructose. Then the dehydration reaction where fructose is converted to 5-HMF and the hydration reaction where furfural is converted to levulinic acid, both catalyzed by sulfonate groups. The simultaneous hydrolysis of cellulose and isomerization of glucose are what increase the overall efficiency of the catalyst to produce levulinic acid [37].

4. CONCLUSION

The present study shows that the higher sulfonation temperature, the more contaminants are lost and volatile materials are released, so that fixed carbon increases and acidity of the catalyst can be higher. In addition, the acidity of the catalyst tends to increase with increasing H_2SO_4 concentration, which means that more sulfonate groups are bound to the surface of the activated carbon. The highest acidity of the sulfonated activated carbon catalyst was obtained at a sulfonation temperature 150℃ and H_2SO_4 concentration of 10 N. Meanwhile, in the performance test for levulinic acid production, the largest cellulose conversion and levulinic acid yield was obtained in cellulose hydrothermal using Ni/SAC catalyst, which was 42% and 4.47%. Overall, the results of this work can provide preliminary report regarding the potential of sulfonated activated carbon catalysts for the production of levulinic acid.

ACKNOWLEDGEMENTS

This research was financially supported by the Faculty of Engineering, Diponegoro University, Indonesia through Strategic Research Grant 2024.

REFERENCES

[1] M. Rai, A. P. Ingle, R. Pandit, P. Paralikar, J. K. Biswas, S. S. da Silva, (2018), 1–26. DOI:10.1080/01614940.2018.1479503

[2] I. Ogino, Y. Suzuki, S. R. Mukai, (2017). http://dx.doi.org/10.1016/j. cattod.2017.10.001

[3] J. R. H. Panjaitan, (2020), 117-123. https://dx.doi.org/ 10.26578/jrti.v14i2.5327

[4] I. B. Okhlopkova, Z. R. Ismagilov, (2020). DOI: 10.1088/1742-6596/1749/1/012008

[5] N. Sweygers, M. H. Somers, L. Appels, (2018), 95-102. https://doi.org/10. 1016/j.jenvman.2018.04.105

[6] M. Zeng, X. Pan, (2020). DOI: 10.1080/01614940.2020.1819936

[7] X. Cao, X. Peng, S. Sun, L. Zhong, W. Chen, S. Wang, R. C. Sun, (2015), 44-51. http://dx.doi.org/10.1016/j.carbpol. 2014.10.069

[8] D. Beyene, M. Chae, T. Vasanthan, D. C. Bressler, (2020). https://doi.org/10.3389/ fchem.2020.00323

[9] S. Kang, J. Ye, J. Chang, (2013), 133-144.

[10] M. M. Zainol, M. N. F. Rosian, M. Asmadi, N. A. S. Amin, (2021), 1-10. DOI: 10.22146/ajche.59865

[11] A. Kristiani, K. C. Sembiring, Y. Aristiawan, F. Aulia, L. N. Hidayati, H. Abimanyu, (2020), 209-215. https://doi.org/10.14710/ jksa.23.6.209-215

[12] Y. Pi, W. Liu, J. Wang, G. Peng, D. Jiang, R. Guo, D. Yin, (2022). DOI: 10.3389/fchem.2022.944398

[13] T. E. Suharto, C. Wulandari, D. Oktiarni, D. Ratnawati, I. Satar, (2022), 107-113. http://dx.doi. org/10.26555/chemica. v9i2.24511

[14] R.N. Yanti, E. Hambali, G. Pari, A. Suryani, (2020), 129-138. DOI: 10.20886/jphh.2020.38.3.129-138

[15] P. Munnik, E. Petra, P. Krijn, (2015), 6687-6718.

[16] E. H. N. L. Gaol, (2023).

[17] C. Li, S. Zhao, M. Li, Z. Yao, Y. Li, C. Zhu, S. Xu, J. Li, J. Yu, (2023), 1-9. DOI: 10.3389/fenvs.2023.976113

[18] W. Trisunaryanti, I. I. Falah, S. K. Nasi'ah, S. D. Sumbogo, (2023), 463-474. DOI: 10.30495/IJC.2023.1992636.2032

[19] A. Yuksel, (2016), 415-434. DOI:10.17482/uumfd.278150

[20] M. A. Ahmad, N. A. A. Puad, O. S. Bello, (2014), 18-35. https://doi.org/10.1016/j.wri.2014.06.002

[21] L. Efiyanti, D. A. Indrawan, D. Santi, S. Wibowo, G. Pari, (2021), 1998-2005. http://doi.org/10.31788/RJC. 2021.1436276

[22] L.J. Konwar, P. I. Mäki-Arvela, J. P. Mikkola, (2019), 11576-11630.

[23] A. Sandouqa, Z. Al-Hamamre, J. Asfar, (2019), 667-682.

[24] A. Aneu, K. Wijaya, A. Syoufian, (2020), 2265-2270. https://doi.org/10.1007/s12633-020-00741-6

[25] L. Efiyanti, Sutanto, N. Hakimah, D. A. Indrawan, G. Pari, (2019), 67-80. DOI: 10.20886/jphh.2019.37.2.67-80.

[26] A. R. O. Ferreira, J. Silvestre-Albero, M. E. Maier, N. M. P. S. Ricardo, C. L. Cavalcante, F. M. T. Luna, (2020). https://doi.org/ 10.1016/j.mcat.2020.110888

[27] M. Guiza, A. Abdedayem, I. Ghouma, A. Ouederni, (2017), 836-851.

[28] G. I. Danmaliki, T. A. Saleh, A. A. Shamsuddeen, (2017), 993-1003. http://dx.doi.org/10.1016/j.cej.2016.10.141

[29] Z. Liu, Y. Qi, M. Gui, C. Feng, X. Wang, Y. Lei, (2019), 5142-5150. https://doi.org/10.1039/C8RA08685K

[30] R. Ediati, A. Mukminin, N. Mukminin, (2017), 30-36. DOI: 10.22146/ijc.23563

[31] I. G. Lee, A. Nowacka, C. H. Yuan, S. J. Park, J. B. Yang, (2015), 12078-12087. DOI: 10.20886/jphh.2020.38.3.129-138

[32] S. Joshi, A. D. Zodge, K. V. Pandare, B. D. Kulkarni, (2014). DOI: 10.1021/ie5011838

[33] D. D. Kulkarni, Purwanto, Rispiandi, (2014), 126-131.

[34] Q. U. Kulkarni, H. Hasanudin, W R. Asri, A. Mara, R. Maryana, S. Gea, K. Wijaya, (2023), 287-309. https://doi.org/10.1007/s11144-022-02334-3

[35] T. Boonyakarn, P. Wataniyakul, P. Boonnoun, A. T. Quitain, T. Kida, M. Sasaki, N. Laosiripojana, B. Jongsomjit, A. Shotipruk, (2019), 2697-2703. http://dx.doi. org/10.1021/acs.iecr.8b05332

[36] Y. Wu, H. Wang, J. Peng, M. Ding, (2023), 92-110. https://doi.org/10.1016/j.cattod.2022.08.012

[37] F. Perveen, M. Farooq, A. Ramli, A. Naeem, I. W. Khan, T. Saeed, J. Khan, (2023), 333-345. https://doi.org/10.1021/ acsomega.2c04545

Malaysian Journal of Catalysis 8 (2024) 58-70

Malaysian Journal of Catalysis
http://mjcat.utm.my/

MJCat
Research Article

An Insight into the Performance and Prospect of Catalysts in Biodiesel Production, with Special Emphasis on Heterogeneous Based Catalysis

Abdu Muhammad Bello[1*]

Department of Chemistry, Faculty of Sciences, Kano University of Science and Technology, Wudil, PMB 3244, Kano State, Nigeria

**Corresponding author: muhbaf70@yahoo.com*

Article history:
Received 01 November 2024
Accepted 23 December 2024

ABSTRACT

Fossil fuel depletion, increased world energy demand, and the environmental crisis linked to petroleum-based energy instigated the quest for its substitute. The sustainability of biodiesel affords it a high prospect over fossil fuels. It has been receiving attention as a result of its biodegradability, renewability, low toxicity, and good transport and storage properties. The main shortcomings of biodiesel are the production cost and choice of catalyst. Three types of catalysts mainly used for biodiesel production are basic, acidic, or enzyme. Industrial production of biodiesel typically employed homogeneous catalysts due to their ability to facilitate the reaction quickly. However, catalyst separation and biodiesel purification are tormenting, requiring a large amount of water. Thus, heterogeneous catalysts, with several advantages over homogenous catalysts, have been searched. Heterogeneous catalysts can be separated from the products effortlessly, thus allowing for recycling. Furthermore, the process is simpler, cheaper, and more environmentally benign. This review aims to evaluate the performance of different types of catalysts in the transesterification reaction, with special emphasis on heterogeneous base catalysts. The review gives insight into the key catalytic properties that need to be tailored economically and eco-friendly to reduce cost, and give better biodiesel yield/conversion. Additionally, the various conditions necessary for the optimum yield of biodiesel have also been explored. The review highlighted that since single and mixed metal oxide catalysts suffered from low activity and instability, modifications need to be done by supporting alkaline or alkaline earth metals in such a manner that the supports hold the catalytic species firmly to achieve good reusability. The review also hinted that although alumina has been an excellent catalyst in many industries, it can only be used as catalyst support in transesterification reaction due to its low activity. The survey further discovered that the use of Nano-sized catalyst with high surface area and enhanced structural properties can help in achieving the key principles in the Green Chemistry. Furthermore, the review suggested solid catalysts, prepared from waste materials, for the reduction of overall biodiesel production cost. Lastly, the future challenges and prospects of heterogeneous base catalysts are proposed.

Keywords: *Biodiesel*, *Catalyst performance*, *Heterogeneous catalyst*, *Transesterification*

| eISSN 0128-2581 |

1. INTRODUCTION

The ever-increasing population growth, urbanization, and economic development continue to raise global energy demand. Further, the over-dependence on fossil fuels; such as coal, oil, and natural gas has significant environmental, economic, and geopolitical consequences [1-2]. These and other factors such as the rapid depletion of fossil fuel reserves, rising oil prices, and growing worries about greenhouse gas emissions in the atmosphere initiated the search for sustainable and environmentally benign alternative energy sources [3-6]. Biodiesel is one such option due to its green nature and other advantages over petroleum-based diesel [7-9]. In an early attempt, over 100 years ago, vegetable oil was proposed by Rudolf Diesel as an alternative to petroleum diesel [10]. However, vegetable oil is highly viscous and thus cannot function well in diesel engines [11]. For this reason, various methods have been investigated in an attempt to reduce the oil's viscosity. This includes pyrolysis, and micro-emulsification, among others [12]. Nevertheless, heavy carbon deposits due to incomplete combustion, coupled with the release of objectionable organic by-products, associated with these two methods have been a setback. Hence, transesterification has been the most efficient method of lowering vegetable oil's viscosity [13].

The transesterification product, known as 'biodiesel', can either be used purely or blended with petro-

diesel [13-15]. The renewability and green nature of biodiesel give it an edge over traditional petroleum diesel [16-17]. Its biodegradability allows for carbon dioxide recycling, thus significantly reducing the greenhouse effect [18]. Furthermore, biodiesel has a high cetane number, and high oxygen content, with no sulfur and aromatic compounds contained, thus their emission is cleaner [19-20]. Additionally, the energy density and kinematic viscosity of biodiesel-diesel blends are similar to the petro-diesel, and hence direct use in the existing engines is feasible [21-22]. The aforementioned advantages have sustained a growing interest in biodiesel production worldwide [23-25]. The global annual biodiesel production increased from 1.0 billion gallons in 2005 to 8.3 billion gallons in 2015 [26].

Catalysts in their simple or complex form, derived from a synthetic or natural source, are usually employed in a chemical reaction to speed it up [27]. Either homogeneous or heterogeneous catalysts can be employed in the production of biodiesel. Homogeneous catalysts used in transesterification reactions comprise HCl, H_2SO_4, NaOH, CH_3ONa, and KOH [28-30]. Nonetheless, homogeneous catalysis is both expensive and harmful due to high energy requirements, corrosion, and excessive use of water in the separation of the product from the catalyst [31-32]. Soap formation resulting from free fatty acids (FFAs} neutralization and triglycerides saponification are other setbacks of homogeneous catalysts.

Table 1: Homogeneous versus heterogeneously catalysts

Factors	Homogeneous Catalyst	Heterogeneous Catalyst
Conversion rate	Fast and high	Moderate
Oil to methanol ratio	Low	High
Continuous packed-bed	limited	Possible
Sensitivity water/FFAs	Not	Sensitive
Reusability	Cannot be reused	Can be reused
Cost	More costly	Cheaper
Selectivity	Limited	Possible

Consequently, heterogeneous catalysts have been introduced to resolve the flaws of homogeneous catalysts [33-34]. Heterogeneous catalysts have the capability of being reused, consequently their application in a packed bed reactor for industrial operation is feasible [35]. Such a reactor reduces the price of biodiesel by eliminating the separation stage [28, 22]. Furthermore, heterogeneous catalysts benefit from high activity, selectivity, and a long catalyst lifetime [36-37]. The homogeneous and heterogeneous catalysts are compared in Table 1 for easy discernment of their advantages and disadvantages. The review focusses mainly on the synthesis of highly efficient heterogeneous catalyst with good stability to enhance biodiesel production. It evaluates the development and production of various heterogeneous base catalysts from different sources including waste materials to reduce biodiesel cost globally. It also envisages the future and prospect of catalysts.

2. MATERIALS AND METHODS

Original research papers (mainly peer-reviewed papers) and reviews were used for this literature survey. The summary of the works consulted in this review according to year of publication is presented in Figure 1 to signify the prevalence of the study. The figure indicates the currency of the review as most of the papers reviewed are within the range of 2015 to 2024 year of publication, with very few old publications, mainly to provide a better understanding of the concept of catalysis in biodiesel production. This justifies the ability of the review in proposing future catalysts that can reduce the biodiesel cost.

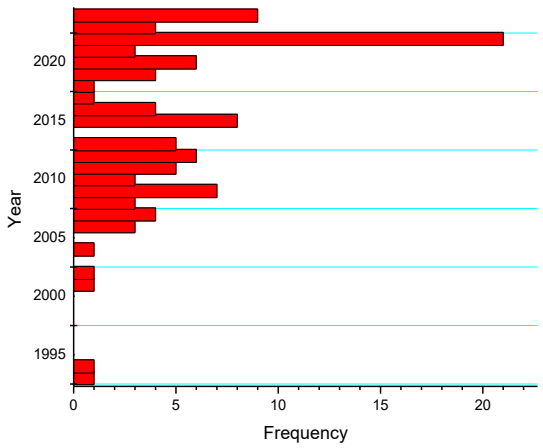

Fig. 1. Bar graph of the reviewed literature

3. BIODIESEL PRODUCTION

The environmental menace connected to fossil fuels, the rise in energy demand, and the decline in fossil fuel reserves, among others, impelled the quest for alternative sources [38-41]. Biodiesel has been proven to be a promising preference for petro-diesel [42-43]. The production of biodiesel is via the transesterification of oils and fats, thus, the emission of greenhouse gases is drastically reduced [44-45]. The methods commonly employed in transesterification are mainly; batch process, supercritical process, ultrasonic method, and microwave method.

Biodiesel is frequently produced by the methanolysis or ethanolysis of high molecular weight fatty acids [35]. Although high molecular weight alcohols, such as isopropanol and butanol, are equally used to boost the

biodiesel's cold flow property, the reaction is less efficient [15]. Some of the advantages of biodiesel are high; flash point, lubricating efficiency, and cetane number with no sulfur content. Furthermore, biodiesel's combustion properties are comparable to petroleum diesel [15,46].

4. TRANSESTERIFICATION REACTION

Transesterification is the alcoholysis of an ester in a process that involves the replacement of its alcohol with another alcohol [47]. Biodiesel was incidentally invented in an attempt to extract glycerol needed for the manufacture of wartime explosives from soap by-products, this research was patented in the early 1940s [48]. The three consecutive and reversible steps involved in the transesterification reaction are presented in Equations 1-3, while the overall reaction is shown in Scheme 1 [49]. The scheme signified that every 1 mole of triglycerides required 3 moles of alcohols to produce 3 moles of biodiesel (alkyl ester) with a mole of glycerol as by product. In addition, heat and catalyst are necessary to speed up the reaction.

$$Triglyceride + ROH \rightleftharpoons Diglyceride + alkyl\ ester \ldots\ldots 1$$

$$Diglyceride + ROH \rightleftharpoons Monoglyceride + alkyl\ ester \ldots\ldots 2$$

$$Monoglyceride + ROH \rightleftharpoons Glycerol + alkyl\ ester \ldots\ldots 3$$

Triglyceride Methanol Glycerol Biodiesel

Scheme 1. Overall transesterification process

Even though, the stoichiometric amount of alcohol in the overall process is three, an excess of 3 moles is necessary to attain a high yield. Despite that, the number of moles of alcohol should not be in too much excess for easy separation of the products [47]. Thus, for homogeneous catalysis 6 moles are suggested, while 15, 40, and 275 are recommended for heterogeneous catalysis to improve the transesterification rate and simplify the catalyst's active site regeneration [50].

4.1 Mechanism of Acid Catalysis in Transesterification

The mechanism of an acid catalyzed biodiesel production is expressed in Scheme 2. The process begins with the protonation of ester to produce carbonion ions. Then the carbonion ion undergoes rearrangement and is in turn attacked by a nucleophile (alcohol) to give a tetrahedral intermediate. This is followed by the elimination of a glycerol to form an alkyl ester (biodiesel). The process is repeated until all the esters are protonated and converted into alkyl esters.

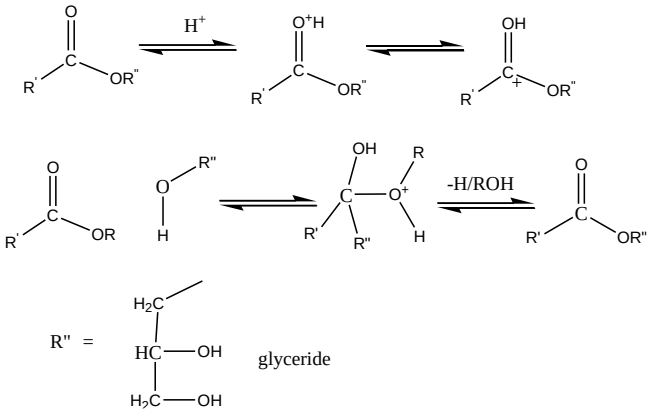

Scheme 2. of acid catalysis in transesterification steps [48]

4.2 Mechanism of Base Catalysis in Transesterification

Due to its faster reaction rate and corrosion free activity, basic catalyst is preferable in industrial processes over the acid counterpart [51]. In this process, the alcohol and catalyst in the reaction mixture react to generate alkoxide ions, initiating the reaction [48]. The various steps involved are illustrated in Scheme 3. Immediately the alkoxide ion is formed. it attacked the triglyceride at C=O double bond and generate an intermediate. This is followed by the elimination of an alkyl ester molecule and regeneration of the catalyst. The process is repeated until all the remaining 3 molecules of the alkyl esters are formed.

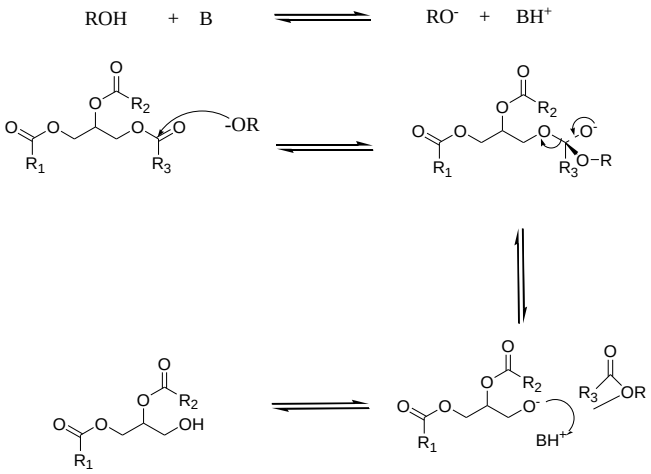

Scheme 3. Outline of base catalysis in transesterification [47].

5. GENERAL MECHANISM OF HETEROGENEOUS CATALYSIS

It is a well-established reality that a catalyst acts by providing an energetically favorable pathway for the

reacting molecules. Generally, the reactants are adsorbed onto the catalyst surface, then the intramolecular bonds are broken or weakened, followed by the reaction of the molecules often in several consecutive steps. For instance, in the oxidation of CO, the catalyst adsorbed the CO and O_2. This is followed by dissociation of the O_2 bond, due to the decrease in potential energy as the adsorption is exothermic, to give two O atoms. Subsequently, the CO and O unite to form adsorbed CO_2 molecules. Finally, the CO_2 molecule is desorbed immediately liberating the catalyst's surface for the next reaction cycle as demonstrated in Figure 2. The regeneration of the catalyst's active sites distinguished catalytic reactions from stoichiometric reactions [52].

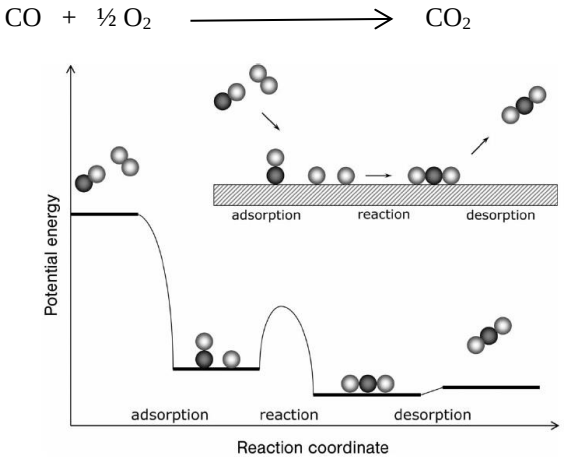

Fig. 2. Catalytic oxidation of carbon monoxide [52]

Similarly, the heterogeneous transesterification mechanism can be explained in the same way. The alcohol adsorbed onto the catalyst surface generating highly active alkoxide ions. The alkoxide ions are then combined with adsorbed glycerides to produce methyl esters. This is followed by instantaneous desorption of the methyl esters, allowing for regeneration of the catalyst's surface. At the commencement of the reaction, the glyceride adsorption is controlled by external mass transfer limitations, while the later reaction is governed by the reaction of the alkoxide ion and TG [52].

6. HETEROGENEOUS ACID CATALYSTS

Heterogeneous acid catalysts were developed to curb, inter alia, the corrosion problems and ensuing environmental threat of homogeneous counterparts. However, the reaction rate of heterogeneous acid catalysts is slow and the reaction is connected with unfavorable side products. Furthermore, understanding the parameters controlling solid acid catalyst activity is still vague. For instance, the relationship between acid strength and catalyst activity is yet to be established. Secondly, even though the synthesis of a heterogeneous acid catalyst having interconnecting pores that will promote transesterification reaction was achieved, the control of the catalyst's pore size, diameter, morphology, as well as stability is not easy [15].

Solid acid catalysts used in transesterification reactions include; zeolites, tungsten oxides, sulfated zirconia (SZ), sulfonated saccharides, Nafion1 resins, phosphoric acid modified mordenite (PMOR), and mesoporous organosulphonic functionalized silica. Although solid acid catalysts are efficient in the esterification of carboxylic acid, lower activity necessitates higher reaction temperatures for their application in the transesterification reaction. However, some resins with a high number of acid sites are exceptional as they have appreciable activity for both carboxylic acid esterification and FFAs transesterification. Nevertheless, thermal stability hinders the application of the resin-type catalysts in reactions, such as reactive distillation, that require higher temperatures. Another concern is associated with catalyst regeneration [15]. Due to all these shortcomings, heterogeneous base catalysts have been introduced. Thus, the current review will be centered on heterogeneous base catalysis in transesterification reactions.

7. HETEROGENEOUS BASE CATALYSTS

Heterogeneous base catalysts came much later than their acid counterparts. The first report on the solid base catalyst was by Pines and Haag. The catalyst composed of Na metal supported on alumina, was found to be efficient in the isomerization of alkenes. The studies on solid base catalysts have made far-reaching progress since the publication of a book by Tanabe, titled “Solid Acids and Bases” [53]. The Brønsted site of heterogeneous base catalyst abstracts proton from the reactant and the Lewis basic site donates an electron to the reactant. Some of the advantages of this catalyst are; higher activity, longer catalyst lifetime, milder reaction conditions, and a reaction rate that is about 4000 times higher than the acid equivalent [47]. The active sites of solid base catalysts can activate reactants with or without proton abstraction.

7.1 Activation of the reactant with proton abstraction

According to Equation 4, the proton of the reactant molecule is abstracted to form carbanion when this molecule is adsorbed on the catalyst surface.

$$\underset{Molecule}{AH} + \underset{Basic\ Sites}{B^-} \rightarrow \underset{Carbanion}{A^-} + BH \ldots\ldots 4$$

For molecules with high pKa values, strong base catalysts are used for easy proton abstraction. For instance, in alkane isomerism, the first step is the abstraction of protons leading to the formation of carbanion as shown in Scheme 4.

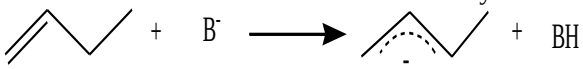

Scheme 4. Activation with proton abstraction

7.2 Activation of reactant without proton abstraction

Carbonyl compounds are usually activated without proton abstraction as shown in Scheme 5. An example of this type of reaction is aldol-condensation.

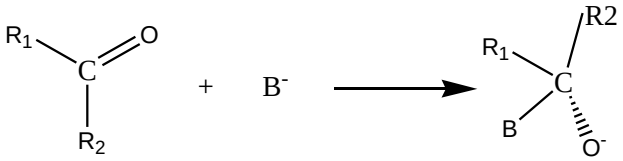

Scheme 5. Activation without proton abstraction

Different categories of heterogeneous basic catalysts are employed in transesterification reaction, details of these catalysts are discussed in the succeeding subsections.

7.3 Metal oxide catalysts

Metal oxide catalysts can either be single (e.g. MgO, CaO, ZnO, etc.), or mixed composed of metal of group I, II, or rare earth metal with transition elements oxides (e.g. $BaCeO_3$). The cation of the metal oxides possesses Lewis acid and the anion possesses Brønsted [54-55]. In a study, Tahvildari *et al* (2015) synthesized Nano CaO and MgO catalysts and evaluated their activity in biodiesel production [56]. The Nano CaO was found to perform better under milder reaction conditions, with higher yield and recyclability than the Nano MgO catalyst. This was connected to the better basicity and surface structure of the Nano CaO. However, when mixed in different proportions with Nano CaO, improvement in the basic properties of the Nano MgO was observed, resulting in an increased biodiesel yield. Accordingly, a 98.95% yield was obtained using a 0.7: 0.5 CaO to MgO mixture, with better repeatability than the Nano CaO alone. In an analogous study, Esmaeili et al., (2019) synthesized MgO nanocatalyst and applied it in the transesterification of low-cost Moringa oleifera seeds oil [57]. The result of the catalyst characterization revealed heterogeneous, asymmetrically distributed small particle sizes. The presence of a great number of pores and inter-mass gaps on the catalyst's surface offers available sites for the transesterification process to occur. Thus, up to 93.69% yield of biodiesel was realized with 1 wt% catalyst, at 45 °C, for 4 h, and a 1:12 molar ratio.

In a related study, Sulaiman *et al*. (2020) synthesized CaO nanoparticles by thermal decomposition of commercial calcium carbonate, CM-$CaCO_3$, under a vacuum atmosphere, by varying the temperature (100 °C to 700 °C) [58]. The FTIR result specified a complete formation of CaO at 700 °C, which is affirmed by the XRD result that revealed peaks exclusively due to crystalline cubic CaO, and the absence of peaks associated with rhombohedral $CaCO_3$ plus hexagonal $Ca(OH)_2$. Interestingly, the surface area and basicity, respectively 11.5 m^2g^{-1} and 1.959 mmol/g, are the highest for the CaO-700 catalyst. The high basicity was attributed to an increase in O^{2-} centers at elevated temperatures of calcination, due to the elimination of OH centers that covered the CaO nanoparticles' surface. When tested in rice bran oil methanolysis, up to 89.0% yield was achieved in 60 minutes, with only 0.5% catalyst amount. In a parallel study, methanolysis of *Balanitea egyptiaca* (Desert date) seeds oil catalyzed by CaO was reported. The yield reached 96.3% with 0.4% catalyst loading, at 55 ºC, for 1 h. The high biodiesel yield was confirmed by the FTIR spectrum of the biodiesel that depicted a sharp band of O-CH_3 around 1033 cm^{-1}. This peak was absent in the Desert date oil spectrum [59]. A similar study reported the synthesis of CaO nano-catalyst using calcium nitrate tetrahydrate as precursor by thermal-decomposition method, the catalyst was calcined at 500 °C followed by characterization using X-ray diffraction (XRD) and scanning electron microscope (SEM) techniques. The XRD results revealed nano-scale crystal sizes with high purity, a mean particle size of around 29 nm, and very good crystallinity.

From the SEM analysis, the catalyst exhibited particles with irregular shapes and porous structures. The catalyst's activity was evaluated in a transesterification reaction, by varying the catalyst's loading and oil: methanol ratio; 0.5 to 5%, and 1: 4 to 1: 10, respectively. The biodiesel yield increased with the catalyst's loading from 0.5 to 1% w/w then declined with further increment, and with molar ratio from 1:4 to 1:8. Consequently, the highest conversion of 96% was achieved at optimized experimental conditions; 50 °C, 1:8 oil to methanol ratio, 1 wt% of catalyst and 90 min reaction time. The work asserted that the reported synthesis method for the nano-CaO catalyst was uncomplicated, entailing only preparation and activation by calcination. Furthermore, it claimed that the catalyst is economical, environmentally benign, and easy to handle, with high basicity and low solubility allowing for the catalyst's reusability [60].

In an attempt to improve the activity and stability of the single metal oxide catalysts research has been shifted to the synthesis of mixed metal oxides. Correspondingly, a study reported the synthesis of mixed CaO-MgO catalyst using the co-precipitation method, to correct the instability associated with CaO and improve its activity. The Mg-doping was varied to determine the best ratio of Mg: CaO for optimum performance. The activity of the different catalysts was investigated in the transesterification of

soybean oil. The characterization results proved the presence of Mg in the doped sample. The Mg doping reduced the lattice spacing of CaO, improved the intensity and number of basic sites, and enhanced the activity of the catalyst, thereby improving the FAME yield from 57.6% for the pure CaO to 98.3% for the Mg-doped CaO catalyst in the ratio of 1: 3, under the reaction condition: 60 ^{o}C, 1: 12 oil: methanol ratio, 1.5 wt% of catalyst, and 2 hrs. reaction time. This was achieved even though supporting MgO on CaO may result in poor pore structure, thus weakening the adsorption and diffusion of reactant molecules to the basic sites, and lowering activity. The optimal performance displayed by 1: 3 Mg: Ca catalyst was credited to higher Mg doping and suitable surface area. The catalysts also proved good stability, as the FAME yield exceeding 80% was maintained after the 5th cycle. The catalyst's stability was attributed to the protection of the basic sites on the catalyst's surface from water and CO_2 contamination by the Mg-doping, which are the main causes of the catalyst's deactivation [20].

Another research by Sahani et al., (2019) reported the synthesis of mixed oxide of barium and cerium by sol-gel method [61]. To investigate the active phase present in the perovskite $BaCeO_3$ catalyst, the calcination time and stoichiometric ratios of Ba: Ce were optimized. Eventually, 1:1 Ba: Ce catalyst calcined for 3.5 hours gave the highest FAME conversion of 98.41% in Karanja oil transesterification using 1.2 wt % catalyst loading, 1:19 molar ratio, 65 °C, 100 min, and 600 rpm agitation speed. The excellent conversion was ascribed to the higher basicity possessed by the catalyst, the maximum exposed area on the catalyst's surface, plus the well-packed and ordered particles of the perovskite that facilitated reactants' adsorption on the catalyst's surface. Furthermore, the catalyst has excellent reusability with 81% conversion after the sixth cycle. This was attributed to the strong intermetallic linkage, Ba-O-Ce, that prevented the leaching of the catalyst. Conversely, the lower activity of the 1:2 Ba/Ce catalyst was attributable to the formation of the inactive CeO_2 phase alongside the active $BaCeO_3$. A similar study reported a green synthesis of GO-$CuFe_2O_4$ nanocomposite as an organo-base functionalized high surface area magnetic nanocatalyst using a mixture of $CuCl_2{\cdot}2H_2O$ and $FeCl_3{\cdot}6H_2O$ as precursors, Graphene oxide (GO) as modifier, and pistachio leaves extract as structure directing agent.

The SEM micrograph of GO-$CuFe_2O_4$ displayed assembled particles and sheet morphology. The EDX result indicated that the catalyst contains Fe and Cu as metallic and C, N, O as non-metallic components. Subsequently, the catalyst was tested in the transesterification of rapeseed oil and waste corn oil. The optimum conditions for biodiesel production were determined through response surface methodology based on Box–Behnken design by varying catalyst loading, methanol to oil molar ratio, and reaction time. The catalyst loading was found to be the most influential parameter for both rapeseed oil and waste-corn oil transesterification. The respective optimum yields of biodiesel for rapeseed oil and waste-corn oil were 92.81% and 87.26%, under reaction conditions: 8 wt% of catalyst, 13:1 methanol: oil molar ratio, and 7 h of reaction time [62]. Table 2 summarizes the various metal oxides catalysts reviewed and the respective optimum biodiesel yields realized.

Table 2: Summary of metal oxides catalysts

Catalyst	Optimum yield (%)	Reference
Nano CaO and MgO	98.95	[56]
MgO Nanocatalyst	93.69	[57]
CaO Nanoparticles	89.0	[58]
Commercial CaO	96.32	[59]
CaO Nanocatalyst	96	[60]
CaO-MgO mixed catalyst	98.3	[20]
$BeCeO_3$ perovskite	98.41	[61]
Graphene oxide GO-$CuFe_2O_4$ nanocomposites	92.81	[62]

7.4 Supported Base Catalysts

During catalyst preparation, supports are modified to hold catalytic species firmly to achieve reusability. The most commonly used catalyst supports include; MgO, CaO, ZnO, and Al_2O_3. Alumina is the most popular among these supports due to its high resistance to heat, large surface area, porosity, mechanical stability, availability, as well as low density, and cost. Due to their super basicity, group I and II metals and their salts, are usually doped onto these supports to improve the number of active sites. For example, when Al_2O_3 was doped with KNO_3, Al-O-K active species were generated by replacing the proton of the $Al(OH)_3$ with K^+ ions, while K_2O are generated by subsequent calcination. The number of basic sites depends on the amount of dopant and the temperature of calcination [28]. The reports on supported base catalysts are discussed in the subsequent paragraphs, while the review intends to take the discussion on alumina-supported basic catalysts into a separate subsection due to their versatility.

A study reported the preparation of nanocrystalline ZnO doped with 2.26% (wt.) potassium by precipitation method. The catalyst gave 89.20% biodiesel yield in rice bran oil transesterification under the RSM model's suggested optimal conditions; 3.60 %wt. Catalyst loading, 65 ^{o}C, 120 mins., and a molar ratio of 6. The researchers concluded that since only 2.26% of K was detected in the biodiesel for the leaching test, the reaction can be considered as heterogeneously catalyzed with very little contribution from the leached K. Consequently, the catalyst was able to be recycled three more times before deactivation [63]. In a parallel study by Roy et al., (2020), La_2O_3 was promoted with potassium and applied in castor oil methanolysis. The

catalyst prepared with a 1.5: 1 atomic ratio of K: La and calcined at 900 °C gave a high conversion of 97.5% with 2 wt% catalysts, 16: 1 molar ratio, at 65 °C, for 150 min, and 500 rpm stirring rate [64]. The generated active K_2O and K_2CO_3 along with the pure La_2O_3 phase, coupled with the homogeneously dispersed and less aggregated particles possessed by the catalyst, contributed to the enhanced basic strength desirable for the transesterification process. Furthermore, the catalyst exhibited good reusability with up to 85.3% FAME conversion after the fifth cycle. The decrease in conversion with catalyst's recycle was attributed to the leaching of K_2O and K_2CO_3.

In a related study by Bambase Jr *et al*., (2021), CaO was wet impregnated with NaOH (10-20%, w/v), and calcined at 550 ^oC - 700 ^oC for 2 - 5.5 h [65]. The catalyst prepared with 20% NaOH, at 600 ^oC for 2 h gave up to 66.36% biodiesel conversion from refined coconut oil in just 10 min, while the reaction catalyzed by untreated CaO took a longer time to commence. The fast reaction rate of the OH-modified catalyst is a result of the high specific surface area originated from the well-shaped lumps of tiny porous particles that served as the basic sites. While the slow catalytic activity of the untreated CaO was attributed to the presence of $CaCO_3$ phase that was believed to compete with the active CaO and $Ca(OH)_2$ in the catalyst's structure. Table 3 is examples of supported base catalysts with their optimum biodiesel yields.

Table 3: Summary of supported base catalysts

Catalyst	Optimum yield (%)	Reference
Zn doped K	89.20	[63]
La_2O_3 promoted with K	97.5	[64]
CaO doped NaOH	66.36	[65]

7.5 Alumina as catalyst support in transesterification

Alumina exists as γ-, η-, σ-, θ-, κ-, χ-, or α-Al_2O_3. Due to its excellent physical, chemical, thermal, and textural properties, alumina has been utilized as a catalyst or catalyst support. These properties permit high doping of active phases [67-69]. Thus, alumina is the most frequently used catalyst support owing to its high surface area and thermal stability. However, alumina has low activity in transesterification reactions, thus, the need to modify its properties for improved activity. On account of its amphoteric nature, both the acid and basic sites of the alumina can be modified [28, 70]. Table 4 portrays a summary of the literature surveys on various acid and base-supported alumina catalysts for transesterification reactions. However, since the review is more concerned with heterogeneous basic catalysis, the later discussion will be on alumina-supported basic catalysts.

Table 4: Generation of Acid and Basic Sites on Alumina

Catalyst	Remark	Reference
$H_4SiW_{12}O_{40}/Al_2O_3$	Acid site	[71]
s-MWCNTs	Acid site	[72]
HSiW-ZrO_2	Acid site	[73]
SO_4^{2-}—ZnO	Acid site	[74]
NiW/SiO_2-Al_2O_3	Acid site	[75]
HSiW/SBA-15	Acid site	[76]
SO_4^{2-}/Al_2O_3-SnO_2	Acid site	[77]
MoO_3/Al_2O_3	Acid site	[78]
Nb_2O_5/ Al_2O_3	Acid site	[79]
Nb_2O_5/Al_2O_3	Acid site	[80]
In_2O_3-Al_2O_3& Ga_2O_3-Al_2O_3	Acid site	[81]
TiO_2/Al_2O_3	Acid site	[82]
KF & $NaNO_3/Al_2O_3$	Basic site	[83]
CaO/KI/Al_2O_3	Basic site	[84]
KI/Al_2O_3	Basic site	[85]
CaO/Al_2O_3	Basic site	[86]
NaOH/Al_2O_3	Basic site	[87]
KF/Al_2O_3	Basic site	[88]
NaOH/Al_2O_3	Basic site	[89]
KI/Al_2O_3	Basic site	[90]
Na/NaOH/γ-Al_2O_3	Basic site	[91]

7.6 Base-supported alumina catalysts in biodiesel production

As earlier highlighted, alumina is the most extensively used catalyst support because of its exceptional thermal, mechanical, and structural properties. Thus, numerous reports are available on base-supported alumina catalysts in the production of biodiesel. One such study by Xie et al., (2006), reported the synthesis of Al_2O_3-supported catalysts by varying amounts of different potassium salts (KF, KCl, KBr, KI) [90]. The Al_2O_3 doped with 35 wt% KI and calcined for 3 h at 500 ^oC was the best catalyst, with up to 96% biodiesel yield, under the conditions of 2.5% of the catalyst, 15:1 molar ratio, and 8 hours reaction time. The higher activity of KI/Al_2O_3 was linked to the lower thermal stability of KI compared to KBr and KCl, resulting in the easy formation of active K_2O species. On the other hand, the superior activity of KI/Al_2O_3 over KF/Al_2O_3 catalyst may be explained by the fact that the active species, F^-, in KF/Al_2O_3, may be weaker than K_2O basic sites. In another study, D'Cruz et al., (2007) promoted alumina with K_2CO_3 and tested it in the methanolysis of canola oil[92]. This catalyst performed better than catalysts prepared by promoting CaO, BaO, and MgO with Li, Na, and K, yielding up to 94.2% ester under the suggested RSM model's reaction conditions of; 11.48:1 molar ratio, 60 ^oC temperature, and 3.16 wt.% catalyst. The high catalytic activity associated with the K_2CO_3/Al_2O_3 catalyst may be attributed to the possession of a much higher surface area of 118 m^2/g, and high basicity. In their study, Arzamendi et al., (2007) prepared calcined

and un-calcined $NaOH/Al_2O_3$ catalysts and compared their activity in sunflower oil methanolysis [89]. The calcined catalyst gave a yield of 86%, while the un-calcined catalyst accomplished a 99% yield, under the same reaction conditions; 12:1 molar ratio, for 24 hours. However, the higher yield achieved with the un-calcined catalyst could be associated with homogeneous contribution due to the non-conversion of the NaOH into Na_2O.

In a parallel study, Boz & Kara, (2009) prepared alumina and modified it with 30 wt.% of KI, KF, K_2CO_3, or KNO_3 [88]. The catalyst modified with KF had the highest activity yielding up to 99.6% biodiesel from canola oil under the conditions; 15:1 molar ratio, 3 wt.% catalyst, 60 ^oC, and 8 hours. The high activity of $KF-Al_2O_3$ was attributed to the high surface area, enhanced basicity, as well as well-dispersed KF that form a monolayer on the alumina. The K_2O and Al-O-K formed by KF decomposition contributed to the high basicity and activity of $KF-Al_2O_3$. Furthermore, Anderson et al., (2009) synthesized BaO/Al_2O_3 catalyst with different baria loading (1, 2.5, 5, and 10 wt.%) and assessed the activities in a transesterification reaction [93]. The result revealed a complex relationship between transesterification reaction and baria dispersion, with low-dispersed samples showing better sensitivity to FFA than poor-dispersed. Accordingly, it was suggested that for high FFA oils, better-dispersed catalysts are more appropriate.

In another study, Istadi et al., (2010) wet-impregnated alumina with different amounts of $LiNO_3$ (10 to 40 wt%) and used it to catalyze palm oil methanolysis [94]. The 20 wt.% $LiNO_3$ catalyst showed well-dispersed particles, resulting in stronger adsorption of reactant, hence, the highest conversion of 97.8 wt% was achieved. For catalysts with less than 20 wt% loadings, the basic sites were very low for the methanolysis reaction to occur. However, when the amount exceeded 20 wt%, the surface area decreased due to particle agglomeration leading to the lowering of the number of basic sites. In a related study, Taufiq-Yap et al., (2011) doped Al_2O_3 with various amounts of NaOH and applied it in palm oil methanolysis [87]. The catalyst prepared with 50 wt% NaOH had the highest yield of 99% when the methanolysis was carried out with 3 wt% catalysts, at 60 ^oC, for 3 hours, and 1:15 molar ratio. Nevertheless, the fact that a high amount of NaOH loading was used in the catalyst's modification, implied a possible homogeneous catalytic contribution to the process. This assertion is true since the study confirmed the formation of sodium aluminate due to a reaction between the alumina support and high-loaded NaOH.

In an attempt to improve on the single-promoted alumina catalysts, Kim et al., (2004) double promoted γ-Al_2O_3 with varying amounts of Na and NaOH, then tested it in soybean oil transesterification [91]. The $Na/NaOH/\gamma$-Al_2O_3 catalyst doped with 20 wt.% of both Na and NaOH has the highest yield of 94% using a 1 g catalyst and a 9:1 methanol to oil ratio. The high activity was credited to the generation of sodium aluminate from the reaction of sodium hydroxide and the γ-Al_2O_3 support, and the ionization of sodium. In a parallel study, Ma et al., (2008) varied the K and KOH wt.% supported on γ-Al_2O_3 and tested the activities in rapeseed oil methanolysis [95]. The 7.5%-$K/20\%-KOH/\gamma$-Al_2O_3 catalyst gave a maximum of 84.52% yield, using 4 wt.% of the catalyst, 1:9 molar ratio, at 60 ^oC, for 1 hour, and a stirring rate of 270 rpm. The activity of the catalyst was a result of the active orthorhombic β-$KAlO_2$ species formed. Nevertheless, the slow stirring rate employed in this study could be the reason for the not-so-high conversion, since the optimum stirring rate was reported to be around 600 rpm.

A parallel study by Asri et al., (2012) reported the double-promotion of γ-alumina catalysts by the co-precipitation of CaO (10 to 50 wt.%) and Al_2O_3 followed by impregnation with 35 wt% KI [84]. The 30%-CaO/35%-KI/Al_2O_3 calcined at 650 ^oC for 4.5 hrs was the most active catalyst. It gave almost 95% yield using 6 wt% catalysts in the methanolysis of palm oil at 65 ^oC, for 5 h, and a 1:42 oil/methanol ratio. The lower yield with CaO loading exceeding 30% was credited to the covering of the basic sites and the consequent surface area lowering due to particle agglomeration. The fact that the optimum activity was achieved at 650 ^oC calcination temperature was ascribed to the fact that elevated temperature is essential for the removal of surface water and carbon dioxide on the calcium oxide to enhance the number of basic sites. Furthermore, at high temperatures, the Ca^{2+} and O^{2-} on the surface of calcium oxide assumed a coordination state that favored high activity. However, the high molar ratio reported could make biodiesel separation from glycerol difficult.

From the foregoing survey, it is clear that most of the reported literature employed commercial or microporous alumina as support. These aluminas suffer from a low surface area that may hinder catalytic activity. Further, the times reported for the transesterification reaction to complete using these alumina-supported catalysts, as well as the metal oxides and metal oxides-supported catalysts, are unusually high (3 hours and in some cases up to 24 hours). This indicated low catalytic activity and a slow reaction rate. To overcome these setbacks, mesoporous alumina was synthesized and wet-impregnated with 5 to 25% NaOH to ascertain the effect of the catalyst's particle size and number of active sites on the methanolysis of corn oil. The parameters for the methanolysis were optimized using the Box-Behnken Design (BBD) model. As high as 96.1% conversion was obtained with 6% of $15\%-NaOH/Al_2O_3$ catalyst, at 65 ^oC, using a 1:15 molar ratio, within 2 hours of reaction time [96]. The fact that only 15% NaOH was used in the catalyst modification to achieve very high biodiesel yield in a shorter reaction time, affirmed the claim that using mesoporous alumina can improve catalytic activity and accelerate reaction rate. This is true since from the aforementioned pieces of literature 30% and above loading was employed when microporous alumina was used as support. Since the literature established that catalysts

modified with alkali metals usually suffer from leaching of the active site, a leaching test was conducted on this catalyst. The catalyst was found to be moderately stable with only 0.7% of Na_2O leaching. Furthermore, the lixiviation test revealed only a 13.5% FAME yield, thus, the leached Na_2O contributed negligibly to the catalytic process. The study attributed the catalyst deactivation to particle agglomeration observed from the SEM image [97]. Table 5 summarizes the performances of various base supported alumina catalysts.

Table 5: Summary of base supported alumina catalysts

Catalyst	Optimum yield (%)	Reference
KI/Al_2O_3	96	[90]
K_2CO_3/Al_2O_3	94.2	[92]
$NaOH/Al_2O_3$	99	[89]
KI, KF, K_2CO_3, or KNO_3/Al_2O_3	99.6	[88]
BaO/Al_2O_3	Not reported	[93]
$LiNO_3/Al_2O_3$	97.8	[94]
$NaOH/Al_2O_3$	99	[87]
$Na/NaOH/Al_2O_3$	94	[91]
$K/KOH/Al_2O_3$	84.52	[95]
$CaO/KI/Al_2O_3$	95	[84]
NaOH/mesoorous-Al_2O_3	96.1	[97]

7.7 Waste-derived catalysts

High production cost, in terms of feedstock oil and catalyst acquisition, is one of the major challenges facing the global commercialization and acceptance of biodiesel. Consequently, for biodiesel to compete favorably with petroleum diesel economically, attention has been shifted to the use of waste materials as precursors for catalyst synthesis. This practice will not only help in reducing the price of biodiesel but also help in reducing the environmental nuisance caused by the dumping of these wastes, among others [12]. This is because effective solid waste management leads to a healthier environment and the generation of this solid waste is something that cannot be avoided [98]. Along this line, a CaO-doped KF catalyst was prepared starting with eggshells calcination in air at 820 °C for 4 hours, then impregnation with KF. When used in a methanolysis reaction as high as 94.2% FAME yield was achieved with 1 wt% of 5%-KF/eggshell catalyst, at 50 °C, for 1 hour, and a 1:6 molar ratio. The high activity was attributed to an improved saponification resistance and the contribution from the well-distributed $KCaF_3$ active crystals on the catalyst's surface. The F^- in $KCaF_3$ served as a strong Lewis base hence easily obstructing H^+ from CH_3OH to form CH_3O^-. Additionally, the strong Lewis acid Ca^{2+} improved the CH_3O^- adsorption on the KF/eggshell catalyst. Consequently, the CH_3O^- easily attacked the triglyceride, resulting in a high FAME yield. Thus, the study concluded that the catalyst is simple, economical, efficient, and promising [99].

To tailor the structural properties of CaO derived from waste eggshells to improve catalytic activity, a study reported the synthesis of CaO nano-catalyst by calcination of eggshell powder at 900 °C followed by hydration-dehydration treatment. The presence of sharp peaks associated with CaO in the XRD diffractogram confirms the formation of CaO. The XRD result further suggested that the hydration dehydration treatment has a strong effect on the crystallinity and crystalline size of the catalyst. The treatment considerably decreases crystallinity thereby increasing porosity and crystalline size, as a result, the surface area increased. This could be associated with the evolution of water molecules since the removal of the water molecules from the lattice during calcination of the hydrated samples ruptures the crystallites. The EDX analysis revealed calcium and oxygen with respective 54.74 and 39.76 mass percentages are the major constituent of the eggshell-derived CaO nano-catalyst. After the hydration-dehydration treatment, the morphology of the catalyst changed from rod-like to honeycomb-like porous microstructure. Likewise, average particle size was reduced from 21.30 to 13.53 nm, leading to an increase in surface area. The change in morphology with hydration-dehydration treatment could be connected to the release of water molecules during the decomposition of $Ca(OH)_2$, thus creating high porosity and more activity. Besides, the hydration-dehydration treatment leads to more uniform textural properties. Accordingly, the highest biodiesel yield of 94% was obtained at 1:12 oil to methanol molar ratio, 2.5 wt% catalyst loading, 60 °C, and 120-min reaction time. The research emphasized that the synthesis procedure is promising for the development of cheap and green technology [100].

In a recent study, Miladinovic et al., (2020) calcined walnuts shell at 800 °C in air and investigated their activity in sunflower oil methanolysis [101]. The catalyst consisted mainly of CaO, K_2O, and MgO, implying high basic nature. Consequently, above 98% yield was accomplished with 5% catalyst in barely 10 min, at 60 °C, and 1:12 molar ratio. The research concluded that even though the walnut shell ash calcination requires high energy, nevertheless, the heat/electricity generated, and averting of operating cost on walnut shell ash disposal, may reimburse the high energy cost. In another study, Pavlović et al., (2020) developed a novel environment-friendly CaO/FA-ZM catalyst using hydration-dehydration in a miniature autoclave. The active CaO and FA-ZM were derived from waste eggshells and lignite coal fly ash, respectively. When 6 wt% of the catalyst was tested in a methanolysis reaction, very high activity with 97.8% FAME conversion in only 30 min, using a 1:6 molar ratio, at 60 °C was accomplished. The uniformly distributed active CaO on the catalyst's surface that drastically improved its basic strength was the origin of the high catalytic activity. Additionally, the negligible drop in activity after the fifth reaction cycle proved the catalyst's stability and was credited

to the integration and stabilization of the active CaO on the FA-ZM support.

Another study reported the preparation of a carbon-based catalyst by the pyrolysis of flamboyant pods followed by functionalization and activation with potassium hydroxide, citric acid, tartaric acid, sulfuric acid, and calcium nitrate to modify either its acidic or basic sites. The catalysts were employed in the methanolysis of safflower oil. Due to its highest specific surface area and potassium and calcium moieties contents, as confirmed by BET and XRD analyses, the alkaline catalyst prepared with potassium hydroxide and calcium nitrate achieved the highest FAME yield of 95% under the following reaction conditions; 5wt% of the catalyst, methanol to oil ratio of 15:1, at 60 °C, for 5h, at a stirring rate of 600 rpm. The catalyst also possessed enhanced stability with 62.2% biodiesel yield after the fourth reaction cycle [7].

Table 6: Summary of base supported alumina catalysts

Catalyst	Optimum yield (%)	Reference
CaO-doped KF (from eggshells)	94.2	[99]
CaO Nanocatalyst (from eggshells)	94	[100]
Calcine walnut shell	98	[101]
CaO/FA-ZM (from eggshells and lignite coal fly)	97.8	[102]
Activated carbon-based catalyst	95	[7]
Mixed CeO_2 (from rare earth hydroxide)	90.42	[34]

Another study reported the synthesis of mixed CeO_2 catalysts utilizing mixed rare earth hydroxide obtained from Thai monazite mineral concentrate as a precursor by co-precipitation method. The performance of these catalysts was optimized in the presence of 10 wt% oleic acids via simultaneous esterification and transesterification of palm oil to biodiesel with 3 wt% of catalyst, 1: 20 oil: methanol molar ratio, at 200 ^oC, for 3 hrs., and 600 rpm stirring speed. The XRF results revealed that CeO_2 ranging between 50–67 wt% was the main component of all the synthesized catalysts, with various amounts of Nd, Y, Sm, Pr, Gd, Er, Dy, and La. The effect of varying temperature, stirring speed, and pH of the precipitation was studied to tune the physico-chemical properties of catalysts. Catalyst synthesized at pH 9 and 30 ^oC reaction temperature under 400 rpm stirring speed was with the highest surface area of 177 m^2/g and possessed a pore volume of 0.19 cm^3/g with small particle size. It was composed of small-large irregular crystallites accumulating together depicting surface roughness. The study concluded that the surface roughness was the reason for the large specific surface area of the catalysts which in turn exposed active sites, leading to an increase in the number of catalytic sites accessible for reaction. Indeed, this catalyst gave the highest FAME yield of 90.42%. The work attributed the high FAME yield to the large surface area of the catalyst, the significantly larger amount of Ce and La contents in the catalyst, and the appropriate amount of acid and basic sites on the catalyst [34]. Table 6 summarizes the preparation of waste-derived heterogeneous catalysts and their efficiencies in biodiesel production.

8. CONCLUSION

The review has focused on different heterogeneous catalysts used in transesterification reactions. Additionally, the yields/conversions from these catalysts were examined. Finally, the various conditions necessary for the optimum yield of biodiesel have also been explored. Single and mixed metal oxide catalysts commonly used in transesterification reactions suffered from low activity and stability. Thus, they are modifikingkamkikied by supporting alkaline and alkaline earth metals to improve the active species for efficient biodiesel production. The review highlighted that the modification should be done in such a manner that the supports hold the catalytic species firmly to achieve good reusability.

The review also hinted that owing to its exceptional stability and outstanding textural properties, alumina is an excellent catalyst in many industries. Conversely, alumina was reported to have low activity in transesterification reactions, hence, it has been mostly used as catalyst support. The survey further discovered that the majority of the literature employed commercially available alumina as catalyst support. This alumina suffered from low surface areas which resulted in lower catalytic activity. Thus, the use of Nano-sized alumina as catalyst support with high surface area and enhanced structural properties was recommended. Finally, the review explored solid catalysts prepared from waste materials, all to suggest ways of reducing the overall biodiesel production cost.

9. CURRENT STATUS, FUTURE CHALLENGES AND PROSPECTS

Although solid acid catalysts are efficient in producing biodiesel from feedstocks with high FFA contents, however, in addition to them having slow reaction rate, understanding the parameters controlling solid acid catalyst activity is still vague. This necessitate the introduction of solid basic catalysts, which helps in ensuring biodiesel prominence. Notwithstanding, recent environmental and socio-economical challenges have brought about new demands which require novel catalysts. It should be noted that, one key challenge in designing such catalysts is achieving phase-homogeneous solids with

uniform morphological and chemical properties. Consequently, the design of catalyst is focusing on that.

Furthermore, the current design of catalysts based on the nanomaterials approach offers new tools for chemical process integration at the nanoscale level. Nano-catalysis guarantees the design of chemical plants that can achieve better integration of units to conserve energy and raw materials. This sustainable process offers optimized direct chemical transformation of raw materials into desired products. In addition to minimizing energy consumptions, waste generation, and environmental hazards, utilization of Nano-catalysis also improved process safety, which are the key principles in the Green Chemistry and Engineering approach.

Future advances should lead to the design of novel catalysts that take advantage of self-assembly of catalytic sites in predetermined two- and three-dimensional configurations. Forthcoming researches should also bridge the different catalysis areas: bio-catalysis, homogeneous and heterogeneous catalysis, together by combining the high selectivity of homogeneous cluster catalysts with the stability and versatility of supported heterogeneous catalysts, which in some cases has already shown its potential. Lastly, chemo-enzymatic new reaction routes will have a great impact on chemical manufacturing in the future.

REFERENCES

[1] Ali, M., Malik, I., Zeeshan, S., & Khubaib, M. (2024) https://doi.org/10.1016/j.ecmx.2024.100675

[2] Singh, Y., Singh, N. K., Sharma, A., Lim, W. H., Palamanit, A., & Alhussan, A. A. (2024) 1–24. https://doi.org/10.1063/5.0214438

[3] Boz, N., Kara, M., Sunal, O., & G, N. D. E. (2009) 433–442. https://doi.org/10.3906/kim-0809-28

[4] Atadashi, I. M., Aroua, M. K., Aziz, A. R. A., & Sulaiman, N. M. N. (2013) 14–26. https://doi.org/10.1016/j.jiec.2012.07.009

[5] Xie, W., Peng, H., & Chen, L. (2006) 24–32. https://doi.org/10.1016/j.molcata.2005.10.008

[6] Julian, A., Rahmandika, P., Rahditya, A., Anggoro, V., Fikri, M., Padmasari, R., Sakinah, Y., & Puspitawati, I. N. (2023) 68–72.

[7] D´ıaz-Muñoz, L. L., Reynel-Avila, H. E., Mendoza-Castillo, D. I., Bonilla-Petriciolet, A., & J´auregui-Rinc, J. (2022) 1–13.

[8] Drieschner, T., Kandelbauer, A., Hitzmann, B., & Rebner, K. (2023) 1–18. https://doi.org/10.32604/jrm.2023.024429

[9] Olatundun, T. O., Popoola, V. A., Fakoyede, P. D., Adebayo, D. O., Kehinde, E. D., Adetoro, Q. A., Akhabue, O. B., & Enabulele, C. (2024) 2054–2081.

[10] Shay, G. E. (1993) 227–242.

[11] Demirbas, A. (2008) 125–130. https://doi.org/10.1016/j.enconman.2007.05.002

[12] Oloyede, C. T., Jekayinfa, S. O., Alade, A. O., Oyetola, O., Otung, N.-A. U., & Laseinde, O. T. (2022) 1–23. https://doi.org/10.1002/eng2.12585

[13] Takase, M. (2022) 1–9.

[14] Lee, D. L. Æ. Y. P. Æ. K. (2009) 63–77. https://doi.org/10.1007/s10563-009-9068-6

[15] Chopade, S. G., Kulkarni, K. S., Kulkarni, A. D., & Topare, N. S. (2012) 8–14.

[16] Luengnaruemitchai, A. (2022) 54–58.

[17] Szkudlarek, Ł., Chałupka-śpiewak, K., Nowosielska, M., Albińska, J., Szynkowska-jóźwik, M. I., & Mierczyński, P. (2024). https://doi.org/10.1016/j.apcato.2024.206999

[18] Yadav, G., Yadav, N., & Ahmaruzzaman, M. (2022) 1–14. https://doi.org/10.1038/s41598-022-25877-w

[19] Spivey, J. J., & Dooley, K. M. (2011).

[20] Hu, M., Pu, J., Qian, E. W., & Wang, H. (2022) 1–32.

[21] Alexandre, J. Y. N. H., Cavalcante, F. T. T., Freitas, L. M., Castro, A. P., & Pedro, T. B. (2022) 1–20.

[22] Bashah, N. A. A., Razali, W. M. Z., Wan, Z., & Rohman, F. S. (2022) 79–89.

[23] Ong, L. K., Kurniawan, A., Suwandi, A. C., Lin, C. X., Zhao, X. S., & Ismadji, S. (2013) 11–20. https://doi.org/10.1016/j.supflu.2012.12.018

[24] Prasad, S., Dhakshinamoorthy, A., & Lalthazuala, S. (2022) 100415. https://doi.org/10.1016/j.ceja.2022.100415

[25] Xie, W., & Li, J. (2023) 113017. https://doi.org/10.1016/j.rser.2022.113017

[26] Guo, M. (2021). Springer India. https://doi.org/10.1007/978-81-322-3965-9

[27] Nagendrappa, G. (2002) 64–77. https://doi.org/10.1007/BF02836172

[28] Stoytcheva, M., & Montero, G. (2011)

[29] Kim, E., Ayuk, A. C., Kim, D.-K., Kim, H. J., & Ham, H. C. (2022) 1–13.

[30] Wongjaikham, W. (2022). 1–22.

[31] Keogh, J., Jeffrey, C., Tiwari, M. S., & Manyar, H. (2022). https://doi.org/10.1021/acs.iecr.2c01930

[32] Zhang, Q., Wang, J., Zhang, S., Ma, J., Cheng, J., & Zhang, Y. (2022) 1–12.

[33] Sivasamy, A., Cheah, K. Y., Fornasiero, P., Kemausuor, F., Zinoviev, S., & Miertus, S. (2009) 278–300. https://doi.org/10.1002/cssc.200800253

[34] Kingkam, W., Issarapanacheewin, S., & Nuchdang, S. (2022) 857–870. https://doi.org/10.1016/j.egyr.2022.10.169

[35] Cristina, H., Gonçalves, A., Miranda, A., & Souza, T. (2022) 34614–34626. https://doi.org/10.1039/d2ra06923g

[36] Xu, C., & Liu, Q. (2011) 1072–1082. https://doi.org/10.1039/c1cy00022e

[37] Taslim, I., Bani, O., Aldi, A., & Rahmadani, S. (2022). 1–6. https://doi.org/10.1088/1755-1315/1115/1/012081
[38] Veljkovic, V. B., Stamenkovic, O. S., Todorovic, Z. B., Lazic, M. L., & Skala, D. U. (2009) 1554–1562. https://doi.org/10.1016/j.fuel.2009.02.013
[39] Tariq, M., Ali, S., & Khalid, N. (2012) 6303–6316.
[40] Araby, R. El, Ibrahim, M. A., Abdelkader, E., & Ismail, E. H. (2022) 1–13. https://doi.org/10.1038/s41598-022-10596-z
[41] Sangian, H. F., Paendong, M. P., Rombang, J. R., Lametige, J. I. L. A., Pasau, G., Bobanto, M., Purwadi, R., & Thahir, R. (2022) 405–416. https://doi.org/10.37394/232015.2022.18.40
[42] Samudrala, S. P., Kandasa, S., & Bhattacharya, S. (2018) 1–12. https://doi.org/10.1038/s41598-018-25787-w
[43] Lin, C., & Tseng, S.-L. (2024) 1–13.
[44] Choghamarani, A. G., Taherinia, Z., & Tyula, Y. A. (2022) 1–12. https://doi.org/10.1038/s41598-022-14341-4
[45] Oshomogho, F. O., & Okologume, W. C. (2024) 50–61.
[46] Sayed, M. A., Ahmed, S. A., Othman, S. I., Allam, A. A., Zoubi, W. Al, Ajarem, J. S., Abukhadra, M. R., & Bellucci, S. (2023)
[47] Kumar, A., Osembo, S. O., Namango, S. S., & Kiriamiti, K. H. (2012) 9–68.
[48] Ejikeme, P. M., Anyaogu, I. D., Ejikeme, C. L., Nwafor, N. P., Egbuonu, C. A. C., Ukogu, K., Ibemesi, J. A., Chemistry, I., & Polytechnic, F. (2010) 1120–1132.
[49] Lee, G., Lee, C., Kim, H., Jeon, Y., Shul, Y., & Park, J. (2022) 1–11.
[50] Kaur, N., & Ali, A. (2015) 193–202. https://doi.org/10.1016/j.apcata.2014.10.013
[51] Guerrero-muñoz, M. A., Mares-molina, K. E., Tovar-negrete, J. J., & Barroso-muñoz, F. O. (2024) 55–60. https://doi.org/10.3303/CET24110010
[52] Niemantsverdriet, J. (2007) Wiley-VCH.
[53] Ono, Y., & Hattori, H. (2011) https://doi.org/10.1007/978-3-642-18339-3_5
[54] Liu, Q., Wang, A., Wang, X., & Zhang, T. (2007) 35–44. https://doi.org/10.1016/j.micromeso.2006.10.011
[55] Kawashima, A., Matsubara, K., & Honda, K. (2008) 3439–3443. https://doi.org/10.1016/j.biortech.2007.08.009
[56] Tahvildari, K., Anaraki, Y.N., Fazaeli, R., Mirpanji, S., Delrish, E. (2015) 73–81.
[57] Esmaeili, H., Yeganeh, G., & Esmaeilzadeh, F. (2019) 257–263. https://doi.org/10.1007/s40089-019-0278-2
[58] Sulaiman, N. F., Yacob, A. R., & Lee, S. L. (2020) 62–69.
[59] Kabo, S., Ogbesejana, A. B., & Bello, A. M. (2020) 132–137
[60] Anbessie, T., Mamo, T. T., & Mekonnen, Y. S. (2019) 1–8. https://doi.org/10.1038/s41598-019-55403-4
[61] Sahani, S., Roy, T., & Sharma, Y. C. (2019) 117699. https://doi.org/10.1016/j.jclepro.2019.117699
[62] Tamoradi, T., Kiasat, A. R., Veisi, H., & Nobakht, V. (2022) 1–15. https://doi.org/10.1038/s41598-022-20538-4
[63] JKabo, K. S., Bello, A. M. and Yalwa, I. R. (2019)103–114.
[64] Roy, T., Sahani, S., & Sharma, Y. C. (2020) 117644. https://doi.org/10.1016/j.fuel.2020.117644
[65] Bambase Jr, Manolito E., Almazan, Rober Angelo R. Demafelis, Rex B., Sobremisana Marisa J. and Dizon, L. S. H. (2021) 571–578. https://doi.org/10.1016/j.renene.2020.08.115
[66] Yang, H., Liu, M., & Ouyang, J. (2010) 438–443. https://doi.org/10.1016/j.clay.2009.12.021
[67] Yang, H., Liu, M., & Ouyang, J. (2010) 438–443. https://doi.org/10.1016/j.clay.2009.12.021
[68] Shi, Z., Jiao, W., Chen, L., Wu, P., Wang, Y., & He, M. (2016) 253–261. https://doi.org/10.1016/j.micromeso.2015.11.064
[69] Xu, N., Liu, Z., Bian, S., Dong, Y., & Li, W. (2016) 4072–4079. https://doi.org/10.1016/j.ceramint.2015.11.079
[70] Sepehri, S., Rezaei, M., Garbarino, G., & Busca, G. (2016) 3456–3464. https://doi.org/10.1016/j.ijhydene.2015.12.122
[71] Liu, L., Wang, B., Du, Y., & Borgna, A. (2015) 32–41. https://doi.org/10.1016/j.apcata.2014.10.017
[72] Hoong, S., Poh, E., & Huat, S. (2015) 1–9. https://doi.org/10.1016/j.jtice.2015.02.018
[73] Talebian-Kiakalaieh, A., & Amin, N. A. S. (2015) 315–324. https://doi.org/10.1016/j.cattod.2015.01.045
[74] Istadi, I., Anggoro, D. D., Buchori, L., Rahmawati, D. A., & Intaningrum, D. (2015) 385–393. https://doi.org/10.1016/j.proenv.2015.01.055
[75] Hanafi, S. A., Elmelawy, M. S., El-Syed, H. A., & Shalaby, N. H. (2015) 27–37.
[76] Chen, Y., Cao, Y., Suo, Y., Zheng, G. P., Guan, X. X., & Zheng, X. C. (2015) 186–192. https://doi.org/10.1016/j.jtice.2015.01.008
[77] Prasitturattanachai, W., & Nuithitikul, K. (2013) 821–825.
[78] Kitano, T., Okazaki, S., Shishido, T., Teramura, K., & Tanaka, T. (2013) 21–28. https://doi.org/10.1016/j.molcata.2013.01.019
[79] Shishido, T., Kitano, Æ. T., Teramura, K., & Tanaka, T. (2009) 383–386. https://doi.org/10.1007/s10562-008-9837-2
[80] Abdel-rehim, M. A., Carlota, A., Santos, B., Camorim, L., Faro, C., & Lu, V. (2006) 211–218. https://doi.org/10.1016/j.apcata.2006.03.023
[81] Haneda, M., Joubert, E., Me, J., Barbier, JDuprez, D.,

Bion, N., Daturi, M., Saussey, J., & Lavalley, J. (2001) 1366–1370. https://doi.org/10.1039/b009945g
[82] Toba, M., Mizukami, F., Niwa, S., & Kiyozumi, Y. (1994) 585–589
[83] Islam, A., Hui, Y., Chu, C., Ravindra, P., & Chan, E. (2013) 23–29. https://doi.org/10.1016/j.renene.2013.01.051
[84] Asri, N. P., Savitri, S. D., & Budikarjono, K. (2012) 116–121. https://doi.org/10.7763/IPCBEE.
[85] Evangelista, J. P. C., Chellappa, T., Coriolano, A. C. F., Fernandes, V. J., Souza, L. D., & Araujo, A. S. (2012) 90–95. https://doi.org/10.1016/j.fuproc.2012.04.028
[86] Umdu, E. S., & Seker, E. (2012) 178–181. https://doi.org/10.1016/j.biortech.2011.11.135
[87] Taufiq-Yap, Y. H., Abdullah, N. F., & Basri, M. (2011) 587–594.
[88] Boz, N., & Kara, M. (2009) 80–92. https://doi.org/10.1080/00986440802301438
[89] Arzamendi, G., Campo, I., & Argui, E. (2007) 123–130. https://doi.org/10.1016/j.cej.2007.03.049
[90] Xie, W., & Li, H. (2006) 1–9. https://doi.org/10.1016/j.molcata.2006.03.061
[91] Kim, H., Kang, B., Kim, M., Moo, Y., Kim, D., Lee, J., & Lee, K. (2004) 315–320. https://doi.org/10.1016/j.cattod.2004.06.007
[92] D'Cruz, A., Kulkarni, M. G., Meher, L. C., & Dalai, A. K. (2007) 937–943. https://doi.org/10.1007/s11746-007-1121-x
[93] Anderson, J. A., Beaton, A., Galadima, A., & Wells, R. P. K. (2009) 213–218. https://doi.org/10.1007/s10562-009-0051-7
[94] Istadi, I., Pramudono, B., Suherman, S., & Priyanto, S. (2010) 51–56.
[95] Ma, H., Li, Æ. S., Wang, Æ. B., Wang, R., & Tian, Æ. S. (2008) 263–270. https://doi.org/10.1007/s11746-007-1188-4
[96] Bello, Abdu Muhammad; Yacoba, Abdul Rahim; Kabo, K. S. (2017) 35–40.
[97] Bello, A. M., Kabo, K. S., Sagagi, B. S., & Yacob, A. R. (2020) 1–7
[98] Ajoke, A. A., Oboho, E., & Emenka, B. (2024) 98–107.
[99] Aziz, M.A.A; Triwahyonob, S. Jalila, A. A. R. H. A. A. and A. A. E. (2016) 22–26.
[100] Erchamo, Y. S., Mamo, T. T., & Workneh, G. A. (2021) 1–12. https://doi.org/10.1038/s41598-021-86062-z
[101] Miladinovic, M. R., Krsti, J. B., & Stamenkovi, O. S. (2020) 1033–1043. https://doi.org/10.1016/j.renene.2019.09.056
[102] Pavlović, S. M., Marinković, D. M., Kostić, M. D., & Janković-častvan, I. M. (2020) 117171. https://doi.org/10.1016/j.fuel.2020.117171

Malaysian Journal of Catalysis
http://mjcat.utm.my/
MJCat
Research Article

Photocatalytic Degradation of Phenol from Textile Wastewater Using Rutile and ZnO-NPs Doped Rutile Nanocomposite

T. L. Adewoye[1], I. A Mohammed[1], S. I. Mustapha[1] H. U. Hambali [1], A. A. Zubairu, A. S. Atanda[1], R. N. Etim [1], and B. K. Ikusemoro[1]

[1] *Department of Chemical Engineering, University of Ilorin, PMB 1515 Ilorin, Kwara Nigeria*

**Corresponding author: adewoye.tl@unilorin.edu.ng*

Article history:
Received 01 November 2024
Accepted 25 December 2024

ABSTRACT

This research focuses on the photocatalytic degradation of phenol from textile wastewater. The objective is to synthesize and characterize zinc oxide nanoparticles and rutile-ZnO-Nps nanocomposite and compare their degradation performance on phenol from textile wastewater. Zinc oxide nanoparticles (ZnO-Nps) were synthesized via a green method by mixing zinc nitrate hexahydrate with *Mangifera indica* leaf extract. The synthesized nanoparticles were incorporated into rutile (TiO_2), a photocatalyst often limited by its band gap and high recombination rate, to obtain the rutile-ZnO-Nps nanocomposite. The particle size distribution of the synthesised ZnO-Nps was assessed using dynamic light scattering (DLS) and the morphology, surface area of ZnO-Nps, pure rutile, and the rutile-ZnO-NPs nanocomposite were determined using scanning electron microscopy (SEM), and Brunauer-Emmett-Teller (BET) analysis. The photocatalytic potential of rutile and rutile-ZnO-Nps to degrade phenol from textile wastewater was investigated under three conditions: sunlight, UV lamp, and darkness. The SEM results revealed that the materials have good morphological properties and the BET results indicated that the synthesised material have relatively large surface area. The rutile-ZnO-Nps demonstrated superior photocatalytic activity under sunlight and artificial light, with degradation efficiencies of 94.87% and 91.66%, respectively, compared to pure rutile's 86.70% and 83.54%. The kinetics of phenol degradation followed pseudo-second order model suggesting chemisorption involving valence forces by sharing or exchanging electron. The doping of ZnO-Nps into rutile matrix enhanced the photocatalytic activity of the nanocomposite.

Keywords: *Photocatalyst, Pollution, Rutile nanocomposite, Textile, Wastewater*

| eISSN 0128-2581 |

1. INTRODUCTION

Access to clean, safe, and sufficient freshwater is vital for the survival of all living organisms and the health of ecosystems. However, increasing global population, coupled with the expansion of industrial and agricultural activities, poses significant threats to water quality [1-2]. Freshwater accounts for only 2.5% of Earth's total water resources, and less than 1% is readily accessible for human consumption [3]. Daily activities such as urbanization, agricultural operations, and population growth generate approximately two million tons of wastewater, further straining these limited freshwater supplies [4].

Industrial advancements, particularly the discharge of untreated wastewater from major industries, exacerbate water contamination issues [5]. Among these, the textile industry is a notable contributor, generating substantial volumes of wastewater through its processes, including pre-treatment, bleaching, dyeing, and printing [6-7]. Alarmingly, over 80% of wastewater globally is discharged untreated into the environment [1]. Such indiscriminate disposal can have dire consequences for human health and aquatic ecosystems. Industrial wastewater toxins are linked to immunosuppression, reproductive disorders, acute poisoning, and waterborne diseases like cholera, typhoid, gastroenteritis, and diarrhea [8-9]. This underscores the critical need for effective wastewater treatment before discharge.

Textile wastewater is particularly challenging due to its toxicity and resistance to conventional biological treatment methods [10]. Traditional approaches, such as coagulation-flocculation [11], precipitation [12], and adsorption [13-14], are often insufficient for completely breaking down and mineralizing pollutants [15]. Consequently, photocatalytic degradation has emerged as a promising alternative. This method, which involves generating highly reactive species like hydroxyl radicals (OH•), enables the oxidation and conversion of toxic organic pollutants into less harmful substances [18]. It is considered an environmentally friendly, durable, and energy-efficient

solution, especially for treating complex, low-biodegradability wastewater with high pollutant concentrations [16-17]. Research continues to focus on developing advanced photocatalysts to enhance the efficacy of this technique.

Various metal oxide semiconductors, including TiO_2, ZnO, Fe_2O_3, CdS, ZnS, and V_2O_5, are commonly utilized in photocatalysis due to their suitable bandgap energies [19]. Among these, titanium dioxide (TiO_2) nanoparticles stand out as ideal candidates for environmental and energy-related applications. This is attributed to their distinctive properties, such as interconnected porous structures and a large surface area, which enhance their catalytic performance [20]. TiO_2 occurs in three crystalline phases: anatase, rutile, and brookite. However, brookite is rarely synthesized and seldom used as a photocatalyst due to its complex production process [21-22]. The anatase phase has been extensively studied and is preferred for photocatalytic degradation of organic pollutant due to its superior properties for oxidation reactions. In contrast, the rutile phase receives limited attention due to its comparatively lower photocatalytic efficiency.

The wide interest in TiO_2 stems from its remarkable stability, widespread availability, biological inertness, low operating temperatures, high photocatalytic activity, favorable flat-band potential, and hydrophobic nature under various environmental conditions. Additionally, its non-toxic profile makes it a sustainable choice for many applications [10]. However, a significant limitation of TiO_2 is its high electron-hole recombination rate, which reduces energy efficiency and diminishes its quantum yield [19, 23]. Several strategies have been employed to enhance the photocatalytic performance of semiconductors, including introducing dopants, sensitization, supporting them on suitable substrates, and combining different semiconductors to form composites [24]. In this study, the coupling of rutile-phase TiO_2 with ZnO nanoparticles (ZnO-Nps) was investigated to enhance the photocatalytic activity of the resulting composite. While the rutile phase has certain limitations compared to the anatase phase, it offers unique advantages, such as better sunlight absorption, lower electron mobility, and greater stability. Additionally, rutile possesses a higher density, dielectric constant, and oxygen adsorption capacity [25], making it a promising candidate for photocatalytic applications. Despite its potential, research on the photocatalytic activity of naturally occurring rutile ore remains limited.

In this work, ZnO-Nps were synthesized using a green approach that employed *Mangifera indica* leaf extract. These ZnO-Nps were then combined with rutile TiO_2 to form a rutile-ZnO-Nps nanocomposite, which was subsequently tested for the photocatalytic degradation of phenol in textile wastewater. While previous studies [26-28] have extensively focused on modifying anatase TiO_2 for the photocatalytic degradation of various pollutants, no reports, to the best of the authors' knowledge, exist on the synthesis of rutile-ZnO-Nps nanocomposites or their application for phenol degradation in real textile wastewater. This study aims to address this gap by incorporating ZnO-Nps onto rutile-phase TiO_2 to form a novel rutile-ZnO-Nps nanocomposite. The photocatalytic efficiency of pure rutile TiO_2 and the rutile-ZnO-Nps nanocomposite was compared under varying conditions to evaluate their effectiveness.

2. MATERIALS AND METHODS

2.1 Reagents

All the reagents used in this study are of analytical grade with percentage purity in the range of 97-99%, and are used without further purification. Analytical grade ethanol (C_2H_5OH), and Zinc nitrate hexahydrate ($Zn(NO_3)_2{\cdot}6H_2O$) were purchased from Sigma-Aldrich.

2.2 Collection of Sample

Mango (*Mangifera indica*) leaves served as the reducing agent in nanoparticle preparation. The leaves were obtained from disease-free mango trees in University of Ilorin campus, Kwara State. The TiO_2 (rutile) sample ore was obtained from a state in Northern Nigeria. The rutile samples were collected in representative portions, cleaned with acetone, and ground into powder using a pulverizer. The powdered samples were stored in air tight sterile sample bottles for subsequent usage.

2.2.1 *Magnifera indica* leaf extract preparation and phytochemical screening of the extract

To prepare the leaf extract, the obtained *Magnifera indica* leaves were rinsed thoroughly in running water, and then with distilled water to remove the adhered dirt. After drying at room temperature, the leaves were pulverized into fine powder using an electric blender. According to the method adopted by Elumalai & Velmurugan, [29], 20 g of powdered leaf were boiled in 100 mL distilled water for 20 min at 60°C, then cooled to room temperature. The sample was filtered using Whatman filter paper, and the filtrate was analysed for phytochemical properties using standard method described by Gupta et al. [30], and then stored in a refrigerator at 4°C until used.

2.2.2 Synthesis of Zinc oxide nanoparticles (ZnO-Nps)

The ZnO-Nps were synthesized via a green method described by Jayachandran et al [31] with slight modification. Accurately weighed, 1 g of zinc nitrate hexahydrate was added to 10 mL of the *Magnifera indica* leaf extract under steady swirling with a magnetic stirrer. After complete dissolution, the solution was heated at 65°C with a magnetic stirrer until a yellow-like colour paste was formed. The paste was then transferred to a ceramic crucible and calcined for 2 h in a furnace at 400 °C.

2.2.3 Synthesis of rutile-ZnO-Nps nanocomposite

The rutile-ZnO-Nps nanocomposite was prepared using the hydrothermal method. Firstly, 1 g of rutile was mixed with 0.5 g of ZnO-Nps in 10 mL of deionized water. The mixture was sonicated for 15 min and then separated by centrifugation for 20 min at 400 rpm. Next, the wet composite was dispersed in 20 mL of a deionized water/ethanol mixture (1:1 v/v), placed in a Teflon-lined stainless steel reactor (Autoclave), and thermally treated at 120°C for 4 h. The obtained precipitate was allowed to cool to room temperature, washed with deionized water several times, filtered and dried in an oven at 60°C for 2 h. The final product was stored in a sample bottle for subsequent use.

2.3 Characterization of the Synthesized Materials

The synthesized ZnO-Nps were characterised for their particle size distribution using Dynamic Light Scattering (DLS) Zetasizer Ver 7.01. The ZnO-Nps, pure rutile and rutile-ZnO-Nps nanocomposite were characterized for their morphology, using Scanning Electron Microscopy (SEM, Hitachi SU 3500 scanning microscope, Tokyo, Japan) using standard procedure. The particles were coated with gold under vacuum before the SEM analysis. Brunauer-Emmet-Teller (BET) Quantachrome Nova Instrument (version 11.03) was employed to determine the surface area and the pore properties using nitrogen adsorption/desorption method.

2.4 Collection and characterization of textile wastewater

Textile wastewater sample was collected from a textile industry in Lagos, Lagos state south-west, Nigeria and stored in a sealed sterile plastic container in the refrigerator at 4°C. The textile wastewater sample was characterized to determine its physicochemical properties using standard procedures. Hanna Multi-parameter instrument was employed to analyse the pH and Turbidity while the BOD level was determined using dissolved oxygen test kit.

2.5 Photocatalytic Degradation of Textile Wastewater

Degradation experiments were conducted to investigate effect of irradiation time on the degradation of phenol in textile wastewater by adding 1 g of pure rutile to series of 250 mL conical flasks, each containing 100 mL of textile wastewater sample and, the conical flasks were placed in the water-bath shaker at room temperature. The water-bath shaker was placed in a dark cupboard and the samples were shaken for 10-50 min. At a regular 10 min intervals, at the end of each reaction time, each conical flask was removed from the shaker and the textile wastewater sample was filtered to separate the used catalyst. The filtrate was then analysed for residual phenol concentration using the method described in subsequent section. The experiment was conducted under the sunlight, and UV lamp at light intensity of 20 mW/cm^3 and wavelength of 254 nm using the same procedure. This procedure was repeated with rutile-ZnO-Nps nanocomposite under the same condition and the blank experiment was also conducted under the same conditions.

The percentage removal of phenol was calculated using Equation 1

$$\%Removal = \frac{C_o - C}{C_o} \times 100 \quad (1)$$

Where C_o and C are the concentrations of the liquid before and after the degradation.

2.5.1 Total phenolic content determination

The Folin-Ciocalteu reagent was used to determine the total phenolic content in extracts. The total phenolics were quantified as mg/g gallic acid equivalents (GAE) using gallic acid as a standard. In methanol, standard solutions of known gallic acid concentrations were prepared. About 0.5 mL of the wastewater sample was measured into a clean test tube using a micro-pipette. Then, 2.5 mL of 10-fold dilute Folin-Ciocalteu reagent and 2 mL of 7.5% sodium carbonate were added to the sample in the test tube. The mixture was allowed to settle for 30 min, and the settling time had been reached, the absorbance of the mixture was obtained using the UV spectrophotometer set at a wavelength of 760 nm.

3. RESULTS AND DISCUSSION

3.1 Characterization of Textile Wastewater

Before degradation, the physico-chemical properties of the textile wastewater were evaluated to estimate the concentration of selected pollutants (COD, BOD, phenolic concentration, and heavy metals) using standard procedures described in the literature [32-34]. The results are presented in Table 1. Most parameters considered exceeded the permissible levels specified by the Federal Environmental Protection Agency (FEPA). The intense colour, and bad odour in the wastewater is detrimental to the lives of aquatic species. The high COD and BOD levels in water bodies indicate the presence of hazardous organic components. BOD is proportional to dissolved oxygen (DO), whereas COD measures the relative oxygen depletion in wastewater and this was found to be relatively high. The BOD and phenolic content are high due to oxidizable organic and inorganic compounds, and other complex mixtures of chemicals in the wastewater. Therefore, it is essential to treat the textile wastewater before being discharged to the environment to improve the quality of the wastewater and support aquatic life.

Table 1: Pollutant Concentration under different conditions

Parameters	Initial values	After treatment with Pure rutile	rutile-ZnO-Nps	Permissible limit FEPA
Phenol (mg/L)	1.58	0.21	0.01	0.2
Odour	Offensive	Odourless	Odourless	Odourless
Colour	Dark	Clear	Clear	Clear
BOD(mg/L)	105	40	21	50.00
COD(mg/L)	210	75	56	<120
pH	8.12	6.7	7.5	6.0-9.0
Turbidity	0.5	0.42	0.34	-
Lead (mg/L)	0.8	0.4	0.2	0.05
Chromium (III)	0.56	0.43	0.32	0.05

After the treatment of the textile wastewater sample with the pure rutile and the synthesised rutile-ZnO-Nps nanocomposite adsorbent, most of the parameters

considered, except for lead and chromium fall within the permissible limit set by FEPA indicating that both rutile and rutile-ZnO-Nps nanocomposite have good potential for degrading organic pollutants in real textile wastewater while the nanocomposite displayed a better performance. Phenol was found to be considerably high (1.58 mg/L) in the textile wastewater sample, and was chosen as a representative of the pollutants for detailed photocatalytic degradation studies. Phenol is known to be a persistent organic pollutant whose presence in water is toxic to aquatic life, human life as well as other living forms [35].

3.2 Characterization of ZnO-NPs, Pure Rutile and the Composite

The ZnO-Nps was characterised for the particle size distribution using Dynamic Light Scattering (DLS). The ZnO-Nps, pure rutile and rutile-ZnO-Nps nanocomposite were analysed for surface area and morphology using Brunauer–Emmet–Teller (BET) and Scanning Electron Microscope (SEM).

3.2.1 DLS results of ZnO-Nps

The synthesized zinc oxide nanoparticle (ZnO-Nps) was characterized to determine its size distribution using DLS and the result is depicted in Figure 1. The average hydrodynamic diameter of the synthesised ZnO-Nps was found to be within nanometer range. The average particle size distribution of ZnO-Nps was 98.71 nm. Notably, the size distribution exhibited moderate dispersion, reflected by a poly-dispersity index >0.7, indicating the ZnO-Nps nanoparticle stability.

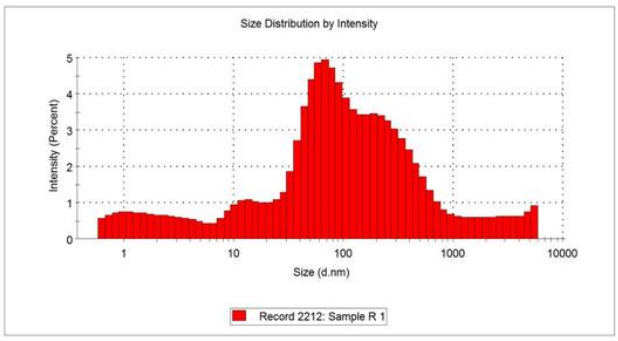

Fig. 1. DLS result for ZnO-NPs

3.2.2 BET analysis of the synthesised materials

The specific surface area, pore volume, and pore size of pure rutile, synthesised ZnO-Nps and rutile-ZnO-Nps nanocomposite were determined using Nitrogen adsorption/desorption method utilizing BET. The BET results revealed that the surface area of ZnO-Nps, rutile and rutile-ZnO-Nps is estimated to be 119.79, 921.1 and 344.52 m^2/g, respectively. The pore volume range from 0.058-0.453 cc/g and pore size was in the range of mesoporous materials (pore radius, $2 \leq r \leq 50$ nm) as specified by IUPAC. The BET results indicated that all the materials studied have good pore properties suggesting high availability of catalytic active sites for higher photocatalytic degradation activity.

3.2.3 SEM analysis of the synthesised materials

Scanning Electron Microscope (SEM) analysis was performed to determine the surface morphology of pure rutile, synthesised ZnO-Nps and rutile-ZnO-Nps nanocomposite and the SEM micrograph is presented in Figure 2. As revealed in the SEM image, the ZnO-Nps (Figure 2a) showed heterogeneous flake-like small particles forming aggregate morphology with opening. The pure rutile (Figure 2b) had a tightly packed structure with no inter-particle gap or lattice stripe. In contrast, more space voids or channels containing particles of nearly uniform sizes were observed in the rutile-ZnO-Nps nanocomposite (Figure 2c). The slight distortion of the rutile arrangement and the appearance of a loosely bound structure may be due to the coupling effect of ZnO-Nps on the rutile matrix [36]. These results suggested that the ZnO-Nps was well incorporated onto the rutile matrix which may be responsible for the better performance displayed by rutile-ZnO-Nps nanocomposite on degradation of phenol in textile wastewater.

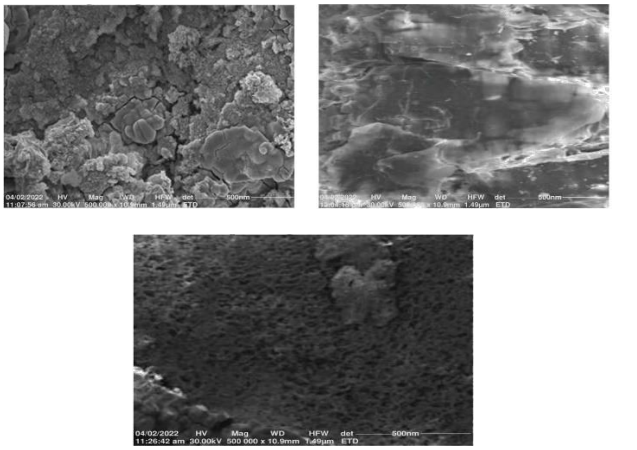

Fig. 2. SEM analysis of (a) ZnO-Nps, (b) Rutile and rutile-ZnO-Nps nanocomposite

3.3 Effect of Time on the Degradation Performance Using Pure Rutile and Rutile-ZnO-Nps nanocomposite

Photocatalytic activity was employed to evaluate the influence of time (10-50 min) on the pure rutile removal efficiency for phenol degradation. The experiment was conducted in a dark cupboard, under artificial light, and natural light irradiations by contacting 1 g of the rutile in 100 mL of textile effluent. At each time interval, samples were taken, and the residual phenol concentration was measured. Figure 3a showed that degradation efficiency increased with time under all three conditions (sunlight, UV, and dark cupboard). In the dark cupboard, removal efficiency increased with time until equilibrium was reached at 40 min,

with a maximum degradation efficiency of 79.74% on phenol degradation. Similarly, Under the UV lamps and sunlight irradiation, the efficiency increased with increase in time and attained equilibrium in 30 and 40 min, respectively with maximum degradation efficiencies of 83.54 and 86.70%, respectively on phenol degradation from textile wastewater. The relatively high degradation efficiency of pure rutile indicated the potentials of rutile TiO_2 to degrade phenol from textile wastewater. This result is comparable with the efficiency reported for phenol degradation using TiO_2 anatase phase by Eddy et al [37]; Yu& Tang [38]

Similar trend was observed with the rutile-ZnO-Nps nanocomposite for the degradation of phenol under the same condition as depicted in Figure 3b. It was noted that under the three conditions considered, the rutile-ZnO-Nps nanocomposite showed a better performance compared with the pure rutile.

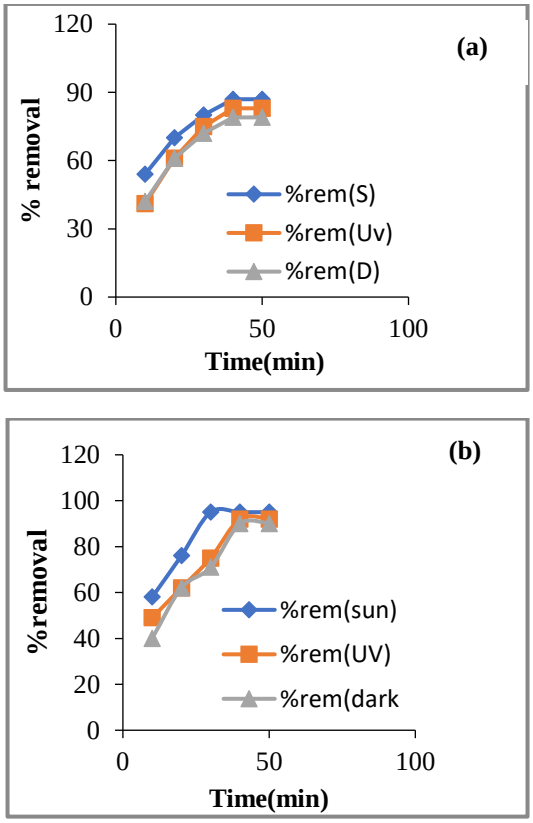

Fig. 3. Effect of time on phenol removal using (a) pure rutile and (b) Rutile-ZnO-Nps nanocomposite

In the dark cupboard, degradation efficiency of the rutile-ZnO-Nps nanocomposite also increased with time until equilibrium was attained at 40 min, achieving a maximum degradation efficiency of 89.74% on phenol. Under UV lamps and sunlight, equilibrium was attained in 30 min and the maximum degradation efficiency of rutile-ZnO-Nps nanocomposite was 91.66 and 94.87%, respectively. The degradation efficiency of the photocatalysts was significantly higher under natural sunlight than artificial light and in the dark cupboard. This may be due to higher intensity of the UV component in sunlight leading to excitation of the photocatalyst and generates more free species, enhancing degradation efficiency under sunlight compared to UV light and in dark cupboard [39]. Furthermore, rutile is known to absorb sunlight quite well, which could potentially explain why it degrades so effectively in the presence of sunlight. It was also observed that the rutile-ZnO-Nps nanocomposite reached equilibrium faster under the sunlight than the pure rutile, an evidence that the coupling of ZnO and rutile significantly enhanced the light absorption leading to an improvement in the photo-degradation efficiency of rutile-ZnO-Nps nanocomposite for degrading phenol in the textile wastewater compared to using pure rutile in agreement with Khan et al. [24] and Asefa et al. [40]. It is interesting to note that the BET surface area of the pure rutile is higher than that of rutile-ZnO-Nps nanocomposite but the results obtained in this study demonstrated that photocatalytic activity of developed catalyst is not dependent only on the surface area of the catalyst. The enhanced degradation efficiency rutile-ZnO-Nps nanocomposite may be due the decrease in electron hole recombination rate [24] as a result of the coupling of rutile with the ZnO-NPs. The combination of rutile and ZnO-Nps allows for improved electron transport from the semiconductor, which prevents recombination and increases the electrons' availability to degrade the phenol from textile wastewater [41].

3.4 Kinetic of Degradation

The kinetic of photo-degradation of phenol in textile wastewater was investigated using Pseudo-first order and pseudo-second order models according to the linear expression presented in Equation 1 and 4, respectively [19]: The kinetic of photo-degradation of phenol in textile wastewater was investigated using Pseudo-first order and pseudo-second order models according to the linear expression presented in Equation 1 and 4, respectively [19]:

$$ln\frac{C}{C_o} = -Kt \quad (2)$$

Equation 2 can be written as the expression Equation 3:

$$ln\frac{C_o}{C} = Kt \quad (3)$$

$$\frac{1}{C} - \frac{1}{C_o} = Kt \quad (4)$$

Where $\frac{1}{C} - \frac{1}{C_o}$ can be represented by $\frac{1}{C_K}$

Where C_o and C are the initial concentration of phenol in textile wastewater and final concentration after time t. K_1 and K_2 are the apparent rate constants for pseudo-first order and pseudo-second order kinetic model. The slope of Plot of $\ln {C}/{C_o}$ $vs\ t$ gives the apparent rate constant K_1 for pseudo-first order model as depicted in Figures 4 and the slope of

the plot of $\frac{1}{C_K}$ vs t gives apparent rate constant K_2 for pseudo-second order model as presented in Figure 5.

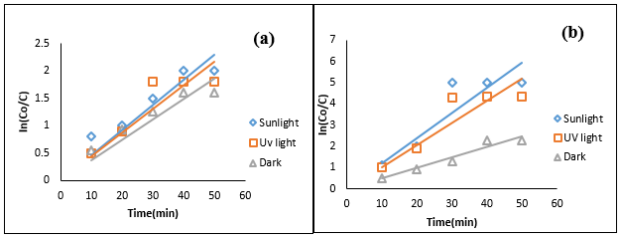

Fig. 4. Pseudo-first order plots of degradation of phenol from textile wastewater using (a) pure rutile; (b) rutile-ZnO-Nps nanocomposite.

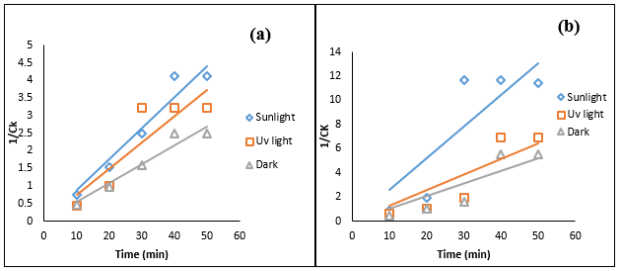

Fig. 5. Pseudo-first order plots of degradation of phenol from textile wastewater using (a) pure rutile; (b) rutile-ZnO-Nps nanocomposite.

The apparent rate constants (K_1 and K_2) and coefficients of determination (R^2) of the phenol photo-degradation under various conditions using pure rutile and rutile-ZnO-Nps nanocomposite were evaluated from Figures 4 and 5, respectively and the results are depicted in Table 2. Comparing the apparent rate constants K_1 and K_2, the K_2 obtained for pseudo-second order kinetic model were higher compared to the K_1 for pseudo-first order kinetic model using pure rutile catalyst and rutile-ZnO-Nps nanocomposite under various conditions as shown in Table 2.

Table 2: Kinetics table for the pure rutile and composite

Catalyst	Models	First Order		Second Order	
	Conditions	K_1(min^{-1})	R^2	K_2 (M^{-1}min^{-1})	R^2
Pure rutile	Sunlight	0.0460	0.7955	0.0881	0.9424
	UV light	0.0435	0.7426	0.0745	0.7895
	Dark cupboard	0.0374	0.799	0.0538	0.9479
rutile-ZnO-Nps nano-composite	Sunlight	0.1184	0.7852	0.2613	0.7367
	UV light	0.1035	0.7919	0.1291	0.7515
	Dark cupboard	0.0489	0.9351	0.1036	0.7658

Though the R^2 value obtained for pseudo-second order using rutile-ZnO-Nps nanocomposite were generally lower compared to that of pseudo-first order, the photocatalytic activity of photocatalysts can be evaluated by comparing the apparent rate constants [40]. This results suggested that the kinetic data were best fitted to the pseudo-second order model which indicated chemisorption involving valence forces by sharing or exchanging electron [42]. The apparent rate constants, K_1 and K_2 obtained for rutile-ZnO-Nps nanocomposite were higher compared to that of pure rutile which further confirmed that the rutile-ZnO-Nps nanocomposite displayed a better performance suggesting that the coupling enhanced the performance of the photocatalyst.

4. CONCLUSION

Zinc oxide nanoparticles (ZnO-NPs) were synthesized from mango leaf extract via a green synthesis route and then incorporated into rutile to produce rutile-ZnO-Nps nanocomposite. The pure rutile and the rutile-ZnO-Nps nanocomposite were characterized and used for the photocatalytic degradation of phenol from textile wastewater. The experiments were conducted under three conditions (in a dark cupboard, under UV light, and sunlight) for both photo-catalysts. ZnO-Nps were successfully synthesized from mango leaf extract and zinc nitrate hexahydrate. The nanoparticles possessed a moderately high surface area, moderate particle size distribution. ZnO-Nps were effective in the synthesis of rutile-ZnO-Nps. The characterization of the synthesized composite showed a very high surface area and pore volume, enhancing its degradation ability. Both rutile and the synthesized composite demonstrated good photocatalytic degradation ability of phenol from textile wastewater under all three conditions (dark cupboard, UV light, and sunlight). The highest removal efficiency was achieved under sunlight for both pure rutile and the rutile-ZnO-Nps nanocomposite. The results revealed that the rutile-ZnO-Nps nanocomposite performed better than pure rutile under all the conditions considered in this study. The maximum removal efficiencies of rutile-ZnO NPs for the degradation of phenol from textile wastewater were 94.87% (sunlight), 91.66% (UV light), and 89.74% (dark cupboard), while those for pure rutile were 86.70% (sunlight), 83.54% (UV light), and 79.74% (dark cupboard). The photocatalytic activity of the prepared samples, irrespective of the irradiation source, follows the order: rutile-ZnO NPs > rutile (TiO_2). The kinetic studies confirmed that the mechanism of phenol mineralization follows a pseudo-first-order kinetic model, which provided the best fit for the experimental data. The synthesised rutile-ZnO-Nps may be employed for effective photocatalytic degradation in the mineralization of textile effluent and other industrial effluents. The use of sunlight as an alternative energy source is considered as an efficient, eco-friendly, and cost effective techniques for photocatalytic degradation.

Hence, future studies could focus optimising the photocatalytic process variables.

REFERENCES

[1] N. Akhtar, M. Syakir Ishak, S. A. Bhawani, K. Umar, (2021) 19.
[2] K. D. Mello, R. H. Taniwaki, F. R. D. Paula, R. A. Valente, T. O. Randhir, D. R. Macedo, C. G. Leal, C. B. Rodrigues, R. M. Hughes, J. (2020)270.
[3] R. K. Mishra, Br. (2023) 3.
[4] J. Fito, S. W. H. Van Hulle, (2021) 3.
[5] T. Jamil, (2024) 318.
[6] N. Sharifi, M. Mohadesi, (2024) 21.
[7] H. Yin, P. Qiu, Y. Qian, Z. Kong, X. Zheng, Z. Tang, H. Guo, (2019) 7.
[8] F. O. Adeola, in: R. Haring, I. Kickbusch, D. Ganten, M. Moeti, (2021) 1–30.
[9] J. Ahmed, A. Thakur, A. Goyal, (2021) 1–14.
[10] A. A. Noaman, (2021) 4351
[11] L. Ayed, I. E. Ksibi, A. Charef, R. E. Mzoughi, (2021) 2.
[12] S. Asha, C. Hentry, M. R. Bindhu, A. M. Al-Mohaimeed, M. R. AbdelGawwad, M. S. Elshikh, (2021) 200.
[13] N. A. Bakar, N. Othman, Z. M. Yunus, W. A. H. Altowayti, M. Tahir, N. Fitriani, S. N. A. Mohd-Salleh, (2021) 22.
[14] J. Fito, S. Abrham, K. Angassa, (2020) 5.
[15] Z., Zheng, S., Tian, Y., Feng, S., Zhao, X., Li, S., Wang, Z., He, Chin. (2023) 54.
[16] A. Nyabadza, M. Makhesana, A. Plouze, A. Kumar, I. Ramirez, S. Krishnamurthy, M. Vazquez, D. Brabazon, (2024) 3.
[17] F. Tanos, A. Razzouk, G. Lesage, M. Cretin, M. Bechelany, (2024) 6.
[18] P. L. Hariani, M. Said, Salni, N. Aprianti, Y. A. L. R. Naibaho, (2022) 23.
[19] M. D. R. Vučić, J. Z.Mitrović, M. M. Kostić, N. D. Velinov, S. M. Najdanović, D. V. Bojić, A. L.Bojić , (2020) 2.
[20] V. Vasanth, K. A. Murugesh, S. Susikaran, (2022) 7. https://doi.org/10.22271/tpi.2022.v11.i7Sd.13643
[21] Z. Heydari, P. Ghadam, (2023) 43.
[22] J. Zhang, P. Zhou, J. Liu, J. Yu, (2014) 38.
[23] M. Aravind, M. Amalanathan, M. S. M. Mary, S (2021) 1 .
[24] S. Khan, A. Noor, I. Khan, M. Muhammad, M. Sadiq, N. Muhammad, (2023) 44.
[25] X. Zhang, J. Chen, S. Jiang, X. Zhang, F. Bi, Y. Yang, Y. Wang, Z. Wang, (2021) 588.
[27] H. Li, Y. Yao, X. Yang, X. Zhou, R. Lei, S. He, (2022) 45.
[28] H. M. El Sharkawy, A. M. Shawky, R. Elshypany, H. Selim, (2023) 1.
[29] K. Elumalai, S. Velmurugan, (2015) 345.
[30] M. Gupta, S. Thakur, A. Sharma, S. Gupta, (2013) 2.
[31] A. Jayachandran, T. R., Aswathy, A. S. Nair, (2021) 26.
[32] J. Ma, S. Wu, N. V. R. Shekhar, S. Biswas, A. K. Sahu, (2020).
[33] S. Mishra, A. Kumar, (2020) 1.
[34] A. Rahman, I. Jahanara, Y. N. Jolly, (2021) 2.
[35] A. I. Lawal, Z. Muhammad, C. V. Obunadike, Y. Y. Yakubu, A. O. Ogunsanmi, O. O. Abdulrazak, C. O. Ayodele, F. E. Komolafe, (2022).
[36] P. Groppe, J. Reichstein, S. Carl, C. Cuadrado Collados, B. Niebuur, K. Zhang, B. Apeleo Zubiri, J. Libuda, T. Kraus, T. Retzer, M. Thommes, E. Spiecker, S. Wintzheimer, K. Mandel, (2024).
[37] D. R. Eddy, S. N. Ishmah, M. D. Permana, M. L. Firdaus. I. Rahayu, Y. A. El-Badry, E. E. Hussein, Z. M. El-Bahy, (2021) 11.
[38] L. Yu, B. Tang, (2021) 16.
[39] J. O. Tijani, U. O. Momoh, R. B. Salau, M. T. Bankole, A. S. Abdulkareem, W. D. Roos, (2019) 19942.
[40] G. Asefa, D. Negussa, G. Lemessa, T. Alemu, J. Nanomater. T (2024).
[41] R. Beura, K. Sooraj, P. Singh, M. Ranjan, S. Mohapatra, (2024) 100595.
[42] H. D. Tran, D. G. Nguyen, P. T. Do, U. N. P. Tran, (2023) 13.